Modelization of Alkali Metal Clusters in Density Functional Theory

Nguyen Van GIAI

Division de Physique Théorique
Institut de Physique Nucléaire, 91406-Orsay Cedex, France
and
Center for Mathematical Sciences, The University of Aizu, Aizu-Wakamatsu, Japan

Different aspects of the physics of atomic clusters are discussed in a common framework, namely the jellium model. The discussion is concentrated on alkali metal clusters. Various versions of the jellium model are examined depending whether the interactions between ions and valence electrons are described by the point-like Coulomb interaction, a pseudopotential or a pseudohamiltonian. These versions lead to different energy density functionals from which one can derive the Kohn-Sham equations describing static properties, and the time-dependent local density approximation (TDLDA) describing excitation spectra of clusters. The numerical solutions of Kohn-Sham equations are used to calculate mean potentials, ionization potentials and shell structure in various clusters as well as supershell phenomena in large ($N \simeq 1000$ - 5000) clusters. Next, the linear response of clusters is studied by solving TDLDA/RPA equations. Calculated dipole plasmons are compared with experimental systematics. The influence of spillout effect and electron effective mass on calculated plasmon energies are also discussed in terms of sum rules. For the limiting case of plasmon in bulk metals with the ion-electron interaction described by a realistic non-local pseudopotential, an analytic calculation shows the lowering of plasmon frequency due to the increase of effective mass. Finally ground state correlations in clusters are examined from two different viewpoints, first by calculating the occupation numbers of electrons in the correlated ground state, and then by looking at the possible existence of harmonic double plasmons. It is found that occupation numbers can depart somewhat from their uncorrelated limits and that strong anharmonicities occur in the multiplasmon spectra, thus indicating strong ground state correlations.

§1. Introduction

The physics of atomic clusters has developed very quickly in the last ten years when experimental techniques have allowed the production of clusters of various sizes ranging from a few atoms up to several hundred atoms or more, and the measurements of their physical properties. The real start was the pioneering work of Knight et al. [1),2)] where evidence of electronic shell structure was found in alkali metal clusters. This gave the basis for the picture where the physics of atomic clusters is essentially governed by the motion of delocalized electrons mutually interacting and undergoing at the same time the influence of a background mean field created by the ions. The relevant degrees of freedom are thus the valence electrons which should be treated by standard many-body techniques while ionic effects could be considered at first approximation in an average way. The detailed spatial distribution of the ions is replaced by a uniform ionic distribution, the jellium which is confined inside a chosen volume.

As for the electron dynamics, it turns out from quantum Monte Carlo calcula-

tions in bulk systems that many-body correlation effects are extremely important and should be introduced somehow. The density functional theory [3] takes into account correlation energy effects by parameterizing the bulk correlation energy obtained in quantum Monte Carlo calculations and adapting it to finite systems by using the local density approximation (LDA). The density functional thus constructed is the starting point of numerous possible applications. The static electronic properties of cluster ground states are obtained by applying the variational principle and solving the related Kohn-Sham equations. Excitation spectra can be calculated in the framework of the so-called time-dependent LDA (TDLDA) which is close to the well-known random phase approximation (RPA). This approach was successfully used to describe the plasmon mode in alkali metal clusters. [4]

In this paper, I shall review some recent theoretical studies of electronic properties of alkali-metal clusters in the framework of density functional theory. This point of view is certainly less fundamental than an *ab initio* approach but it has the great merit of providing a systematic description of clusters of all sizes whereas *ab initio* calculations are practically limited to clusters of less than, or about 20 atoms. I shall also emphasize the importance of treating in a realistic fashion the ion-valence electron interaction by using effective pseudopotentials or pseudohamiltonians in conjunction with the jellium model.

The literature on this subject is rather vast and quickly growing. As a guideline, the reader is referred to the recent experimental survey of de Heer. [5] The jellium model and semiclassical studies of metal clusters are reviewed in Ref. 6).

§2. Jellium models

Let us consider a system of N atoms with Z electrons in each one of them. We shall restrict ourselves to monovalent atoms (alkali metals) but the present general considerations could be extended to atoms with more than one valence electron. We are concerned with an energy domain corresponding to laser beam experiments (optical domain) where only valence electrons can be excited and delocalized while deeply-bound electrons remain in the atomic core. Thus, the cluster can be viewed as a system of N ions and N delocalized (valence) electrons governed by the Hamiltonian:

$$H = H_{ion} + H_{el} \ , \tag{1}$$

$$H_{ion} = \sum_{I=1}^{N} \frac{\boldsymbol{p}_I{}^2}{2M} + \frac{1}{2} \sum_{I \neq J} \frac{e^2}{|\boldsymbol{R}_I - \boldsymbol{R}_J|} \ , \tag{2}$$

$$H_{el} = \sum_{i=1}^{N} \frac{\boldsymbol{p}_i{}^2}{2m} + \frac{1}{2} \sum_{i \neq j}^{N} \frac{e^2}{|\boldsymbol{r}_i - \boldsymbol{r}_j|} + \sum_{i=1}^{N} \sum_{I=1}^{N} V_{e\text{-}i}(\boldsymbol{r}_i - \boldsymbol{R}_I) \ . \tag{3}$$

The first assumption is to neglect the ion dynamics and to consider only the delocalized electrons obeying the Hamiltonian H_{el}. The second assumption is to replace the

actual distribution of ions by a uniform ionic background inside some fixed volume that we shall choose of spherical shape for simplicity (extension of the jellium model to non-spherical shapes can also be done, see, e.g., Ref. 7)). The radius R of the jellium sphere depends on the number of atoms and on the Wigner-Seitz radius r_s which characterizes the particular type of atom:

$$R = r_s N^{1/3} \ . \tag{4}$$

The values of r_s are known from the bulk systems. In Table I are shown the Wigner-Seitz radii of same alkali metals. Here and in the following we use atomic units (a.u.) unless specified otherwise ($e^2 = \hbar = m = 1$; a.u. of length = Bohr electron radius = 0.53 Å; a.u. of energy = 2 Ry = 27.2 eV).

Table I. r_s radii of some alkali metals.

element	Li	Na	K	Rb	Cs
r_s(a.u.)	3.26	3.93	4.86	5.20	5.62

Thus, the ionic background distribution $n(\boldsymbol{r})$ is equal to $n_0 = (4\pi {r_s}^3/3)^{-1}$ inside the jellium sphere and zero outside.

Let us now examine different approximations for the electron-ion term of the Hamiltonian (3). In the plain jellium model (JM) the interaction $V_{e\text{-}i}$ is the Coulomb interaction between two point charges:

$$V_{e\text{-}i}(\boldsymbol{r}_i - \boldsymbol{R}_I) = -\frac{e^2}{|\boldsymbol{r}_i - \boldsymbol{R}_I|} \ . \tag{5}$$

In this case, the last term of (3) is simply:

$$H_{e\text{-}i} = \sum_i \int \frac{-e^2 n(\boldsymbol{r}_I)}{|\boldsymbol{r}_i - \boldsymbol{r}_I|} d^3 r_I \ . \tag{6}$$

Of course, assumption (5) is rather crude. In particular it takes no account of the effects of core electrons in isolated atoms, where realistic pseudopotentials have been constructed in order to reproduce electronic spectra of full core atoms. For instance, Bachelet, Hamann and Schlüter[8] have proposed non-local pseudopotentials of the form:

$$V_{e\text{-}i} = v_{\mathrm{loc}}(\boldsymbol{r} - \boldsymbol{r}_I) + \Delta v(\boldsymbol{r} - \boldsymbol{r}_I, \boldsymbol{r}' - \boldsymbol{r}_I) \ , \tag{7}$$

where

$$\Delta v(\boldsymbol{x}, \boldsymbol{x}') = \sum_{L=0}^{L\max} \sum_M Y_{LM}(\hat{x}) Y^*_{LM}(\hat{x}') v_L(x) \frac{\delta(x - x')}{x x'} \ , \tag{8}$$

and they have determined the parameters of these pseudopotentials for all elements of the periodic table. One can use (7) and (8) to construct an electron-ion Hamiltonian more realistic than (6), at the cost of major practical complications since $H_{e\text{-}i}$ is

now fully non-local in electron coordinates. This has been done nevertheless [9] and the results of this pseudopotential jellium model (PPJM) show distinct improvement over those of JM, especially for Li clusters.

A simplified version of effective ion-electron interactions has also been proposed by Bachelet et al. [10] where momentum-dependent terms are introduced instead of full non-locality. The effective interaction is described by a Hamiltonian of the form:

$$h = v(\boldsymbol{x}) - \frac{1}{2}\nabla_x a(\boldsymbol{x}) \cdot \nabla_x + \frac{1}{2}\boldsymbol{L}_x \frac{b(x)}{x^2} \cdot \boldsymbol{L}_x \ , \tag{9}$$

where $\boldsymbol{x} \equiv \boldsymbol{r} - \boldsymbol{r}_I$ and $\boldsymbol{L}_x$ is the angular momentum operator: $\boldsymbol{L}_x = i\boldsymbol{x} \wedge \boldsymbol{p}$. The functions $a(x)$, $b(x)$ and $v(x)$ can be calculated starting from the pseudopotentials (7) and (8). The potential $v(x)$ goes like $\frac{1}{x}$ at large distance but it is somewhat weaker inside the ion because of screening. An example of effective ion-electron Hamiltonian is shown in Fig. 1 for a K atom and in Fig. 2 for a Li atom. In the latter case the function $a(x)$ takes large values inside and gives rise to a large effective mass. These so-called pseudohamiltonians are easier to use in the framework of a jellium model because non-local effects on the electronic mean field are dumped into a position-dependent effective mass. If one folds $h(\boldsymbol{r} - \boldsymbol{r}_I)$ with the jellium density $n(\boldsymbol{r}_I)$ one obtains the corresponding ion-electron effective Hamiltonian $H_{e\text{-}i}$ which contains, in addition to a potential term similar to (6), momentum-dependent terms which contribute to the crystalline effective mass. Results of this pseudohamiltonian jellium model (PHJM) are generally close to those of the PPJM (except in the case of bulk limit of Li cluster [11]) and better than plain JM. [12] We shall review them in

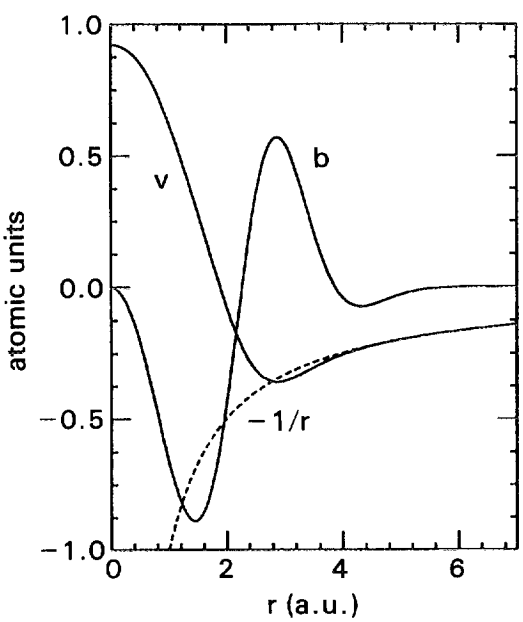

Fig. 1. Pseudohamiltonian functions $b(r)$ and $v(r)$ for the potassium atom. For this element the function $a(r)$ is zero by construction.

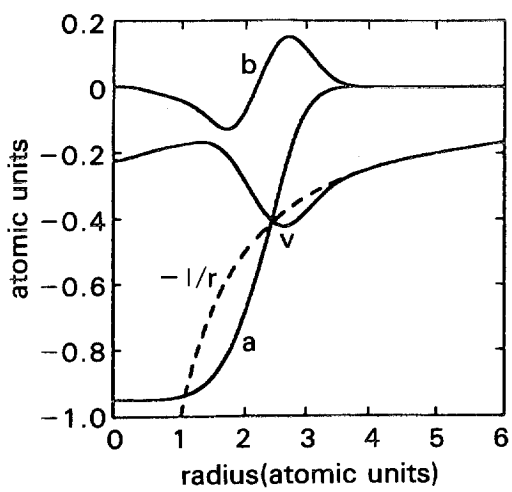

Fig. 2. Same as Fig. 1, for the lithium atom.

the next sections.

With the above choices for $H_{e\text{-}i}$ we can now proceed to construct the energy functional representing the total energy of valence electrons in the cluster. It is expressed as a functional of the local density of valence electrons:

$$E = T[\rho] + E_{es}[\rho] + E_{xc}[\rho] + E_{ei}[\rho] \ . \tag{10}$$

Then, the one-body density $\rho(\boldsymbol{r})$ is determined by means of a variational principle. In the Kohn-Sham approach one assumes the density to be of the form:

$$\rho(\boldsymbol{r}) = \sum_{i=1}^{N} |\phi_i(\boldsymbol{r})|^2 \ , \tag{11}$$

where the ϕ_i are single-particle wave functions of occupied orbitals to be determined by a self-consistent procedure.

The first term in Eq. (10) is the electronic kinetic energy:

$$T = \int \tau(\boldsymbol{r}) d^3r \ , \tag{12}$$

where the kinetic energy density $\tau(\boldsymbol{r})$ is:

$$\tau(\boldsymbol{r}) = \frac{1}{2} \sum_{i=1}^{N} |\nabla \phi_i(\boldsymbol{r})|^2 \ . \tag{13}$$

The second term of Eq. (10) represents the electrostatic energy due to direct Coulomb interactions among valence electrons and it takes the simple form:

$$E_{es}[\rho] = \frac{1}{2} \int \frac{\rho(\boldsymbol{r})\rho(\boldsymbol{r}')}{|\boldsymbol{r} - \boldsymbol{r}'|} d^3r d^3r' \ . \tag{14}$$

The third term of Eq. (10) is the exchange-correlation energy which describes the exchange part of the Coulomb energy between electrons plus all the contributions due to other correlations. The exchange-correlation energy can be expressed in terms of the local density if one makes use of the LDA which consists in adopting for the energy density at point $\boldsymbol{r}$ that of a uniform system of density $\rho = \rho(\boldsymbol{r})$. Thus, the exchange component of E_{xc} is the so-called Slater approximation:[13]

$$E_x[\rho] = -\frac{3}{4} \left(\frac{3}{\pi} \right)^{1/3} \int (\rho(\boldsymbol{r}))^{4/3} d^3r \ . \tag{15}$$

The correlation component of E_{xc} is usually introduced in a parameterized form, the most often used versions being that of Wigner:[14]

$$E_c[\rho] = -\int \frac{0.88}{r_s(\rho) + 7.8} \rho(\boldsymbol{r}) d^3r \ , \tag{16}$$

and of Gunnarsson and Lundqvist:[15]

$$E_c[\rho] = -0.0666 \int \left((1 + x^3) \log \left(1 + \frac{1}{x} \right) - \frac{1}{3} + \frac{x}{2} - x^2 \right) \rho(\boldsymbol{r}) d^3r \ . \tag{17}$$

Expressions (16) and (17) are given in atomic units, and the quantity x in Eq. (17) is $r_s(\rho)/11.4$ where $r_s(\rho)$ is the electronic Wigner-Seitz radius:

$$r_s(\rho) = \left(\frac{3}{4\pi\rho}\right)^{1/3} . \tag{18}$$

We note that expression (14) contains the spurious self-interactions of each electron with itself. These spurious contributions would be exactly cancelled out if the Coulomb exchange energy E_x were calculated exactly as in Hartree-Fock theory. The fact that E_x is treated in LDA invalidates this cancellation. This is the price to pay for obtaining the simplicity of the energy functional approach.

The fourth term of Eq. (10) is the electron-ion energy. In the plain JM it is:

$$E_{ei} = \int \rho(\boldsymbol{r}) V_I(\boldsymbol{r}) d^3r , \tag{19}$$

where $V_I(\boldsymbol{r})$ is the electrostatic potential of the jellium (see Eq. (6)):

$$V_I(\boldsymbol{r}) = -e^2 \int \frac{n(\boldsymbol{r}')}{|\boldsymbol{r} - \boldsymbol{r}'|} d^3r' . \tag{20}$$

In the PHJM, E_{ei} has a form similar to (19) with $V_I(\boldsymbol{r})$ replaced by an operator $\hat{V}_I$ acting on the coordinate $\boldsymbol{r}$:

$$\hat{V}_I(\boldsymbol{r}) = \int n(\boldsymbol{r}') h(\boldsymbol{r} - \boldsymbol{r}') d^3r' , \tag{21}$$

where $h(\boldsymbol{r} - \boldsymbol{r}')$ is the pseudohamiltonian (9) describing the relative motion of an electron with coordinate $\boldsymbol{r}$ and an ion at point $\boldsymbol{r}'$. The calculation of $\hat{V}_I$ can be done directly by making multipole expansions of the functions $a(\boldsymbol{r} - \boldsymbol{r}')$, $b(\boldsymbol{r} - \boldsymbol{r}')$, and $v(\boldsymbol{r} - \boldsymbol{r}')$ appearing in (9). Let us define:

$$\begin{aligned} a(\boldsymbol{r} - \boldsymbol{r}') &= \sum_{LM} a_L(r, r') Y_{LM}(\hat{r}) Y^*_{LM}(\hat{r}') , \\ \tilde{b}(\boldsymbol{r} - \boldsymbol{r}') &\equiv \frac{b(\boldsymbol{r} - \boldsymbol{r}')}{2(\boldsymbol{r} - \boldsymbol{r}')^2} \\ &= \sum_{LM} \tilde{b}_L(r, r') Y_{LM}(\hat{r}) Y^*_{LM}(\hat{r}') , \\ v(\boldsymbol{r} - \boldsymbol{r}') &= \sum_{LM} v_L(r, r') Y_{LM}(\hat{r}) Y^*_{LM}(\hat{r}') . \end{aligned} \tag{22}$$

After some cumbersome but straightforward algebra one obtains, for the case of a spherical jellium:

$$\hat{V}_I = -\frac{1}{2} \nabla \cdot \alpha(r) \nabla + \boldsymbol{L} \cdot \beta(r) \boldsymbol{L} + U_I(r) , \tag{23}$$

where the functions α, β and U_I are:

$$\begin{aligned} \alpha(r) &= A_0^{(2)}(r) + \frac{4}{3} B_0^{(4)}(r) - \frac{4}{3} B_2^{(4)}(r) , \\ \beta(r) &= B_0^{(2)}(r) - \frac{2}{r} B_1^{(3)}(r) + \frac{1}{r^2} B_2^{(4)}(r) , \\ U_I(r) &= V_0^{(2)}(r) \end{aligned} \tag{24}$$

with

$$A_L^{(k)} = \int_0^\infty n(r')a_L(r,r')r'^k dr' \ ,$$
$$B_L^{(k)} = \int_0^\infty n(r')b_L(r,r')r'^k dr' \ ,$$
$$V_L^{(k)} = \int_0^\infty n(r')v_L(r,r')r'^k dr' \ . \tag{25}$$

The PPJM case is somewhat more involved because the jellium averaging of the non-local potential (7) – (8) leads to a non-local potential for valence electrons and therefore E_{ei} involves now the non-local electronic density $\rho(\boldsymbol{r},\boldsymbol{r}')$. We shall not treat in detail the corresponding expressions and we refer the reader to the work of Alasia et al.[9]

§3. Static properties

3.1. *Kohn-Sham equations*

The energy (10) is a functional of the single-particle wave functions ϕ_i since the electronic density ρ and kinetic energy density τ are expressed in terms of the ϕ_i. These wave functions are determined by demanding that E be stationary with respect to variations of the ϕ_i such that their norm is conserved:

$$\frac{\delta}{\delta\phi_i^*}\left[E - \sum_{j=1}^{N}\varepsilon_j\langle\phi_j|\phi_j\rangle\right] = 0 \ , \tag{26}$$

where the ε_j are Lagrange multipliers and the sum runs over occupied orbitals. One thus obtains the Kohn-Sham equations:

$$\left(-\frac{1}{2}\nabla\cdot(1+\alpha(r))\nabla + \boldsymbol{L}\cdot\beta(r)\boldsymbol{L} + U_I(r) + W(\boldsymbol{r})\right)\phi_i(\boldsymbol{r}) = \varepsilon_i\phi_i(\boldsymbol{r}) \ , \tag{27}$$

where

$$W(\boldsymbol{r}) = \int\frac{\rho(\boldsymbol{r})}{|\boldsymbol{r}-\boldsymbol{r}'|}d^3r' + \frac{\delta E_{xc}}{\delta\rho} \ . \tag{28}$$

These modified Kohn-Sham equations for the PHJM are a generalization of the usual equations for the JM which can be recovered by setting $\alpha = \beta = 0$ and replacing $U_I(r)$ by V_I. It must be noted that the PHJM Kohn-Sham equations have a modified kinetic energy operator which, just as in the case of an isolated ion, can be interpreted in terms of a radial and direction-dependent effective mass tensor.[10]

The set of equations (27) must be solved self-consistently by an iterative procedure. Assuming spherical symmetry for the cluster, the equations can be reduced to second order differential equations for the radial parts of the wave functions ϕ_i and then solved numerically using the Runge-Kutta algorithm. When self-consistency is reached, one obtains not only the set $\{\phi_i,\varepsilon_i\}$ of occupied orbitals but also the self-consistent mean field $W(\boldsymbol{r})$ which allows us to calculate the unoccupied orbitals as well. The mean field $W(\boldsymbol{r})$ together with the functions $\alpha(r)$, $\beta(r)$, $U_I(r)$ are essential quantities for TDLDA calculations of excitation spectra as we shall see in §4.

3.2. *Mean potentials, effective mass and densities*

Let us first look at the mean effective potentials coming out of the self-consistent solutions. We take the $N = 40$ case as an illustrative example. In Figs. 3 and 4 are plotted the mean potentials for Li, Na and K clusters calculated in the JM and PHJM, respectively. It can be seen that the shapes are similar in both models. However, the JM potentials approximately scale with r_s as one can check by looking at the values at the origin whereas the PHJM potentials do not. This is due essentially to the existence of effective mass in PHJM. Indeed, the values at origin are almost the same in both models for Na and K clusters where the effective mass is close to 1 while they strongly differ for Li clusters where the effective mass is large. One can also notice that the minimum near the surface, which is related to the maximum of electron density at the same point due to the Friedel oscillations, is less pronounced in PHJM. Consequently, electrons are less bound in PHJM and their polarizability is increased and tend closer to experimental values.[2),16)]

One important change in the Kohn-Sham equations (27) when one introduces the PHJM is that the bare electron mass m becomes a position-dependent effective mass:

$$\frac{m^*(r)}{m} = \frac{1}{1+\alpha(r)} \,. \tag{29}$$

This effective mass depends on the terms $a(\boldsymbol{r})$ and $b(\boldsymbol{r})$ of the pseudohamiltonian (see Eq. (24)) and it is ultimately related to the properties of the particular type of atom involved in the cluster. As an example, we show in Fig. 5 the effective mass in alkali clusters with $N = 20$ atoms.

It can be seen that Li clusters have a rather large effective mass whereas other alkali clusters have values of m^*/m close to, or smaller than unity. The large effective mass in Li clusters explains partly for the fact that the plasmon energy is considerably lower in PHJM than in JM, as we shall see in §4. Indeed, large values of m^* increase the single-particle level density and thus decrease the particle-hole

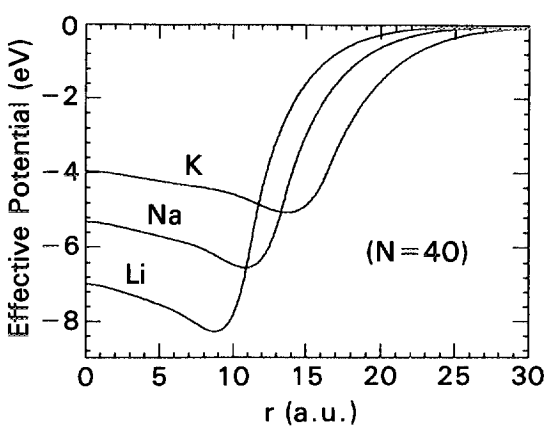

Fig. 3. Mean potentials for Li, Na and K clusters with $N = 40$ atoms, calculated with JM model.

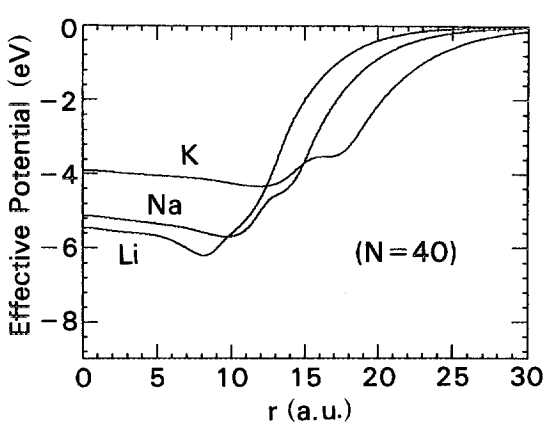

Fig. 4. Same as Fig. 3, with PHJM model.

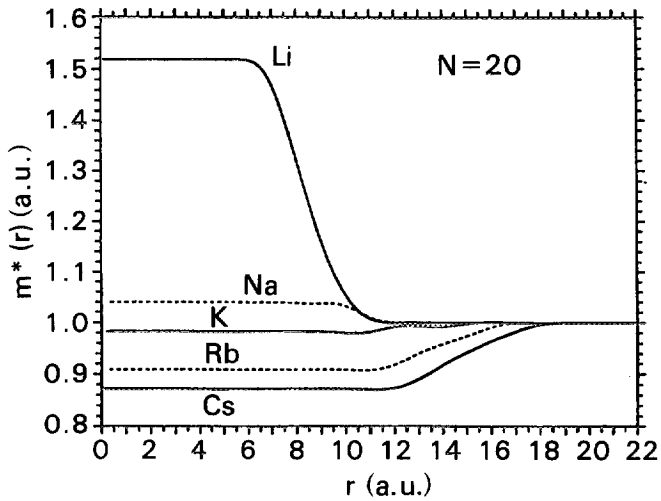

Fig. 5. Effective mass in alkali metal clusters with $N = 20$ atoms, calculated with PHJM model.

excitation energies. It must be noted that, in all alkali clusters the values $m^*(r)$ stay fairly constant in the interior region and that these values do not change much when the size number N is increased.

Let us now briefly discuss the predicted electronic densities. Calculated densities (normalized to n_0 so that the integrals are just the cluster volume) obtained in JM and PHJM are shown in Figs. 6 $\sim$ 8 for K, Na and Li clusters with $N = 40$. In all cases the PHJM densities inside the jellium sphere show smaller oscillations than JM densities. This is a reflection of the reduction of the "Friedel dip" at the surface of the PHJM mean potential. Consequently, the number of electrons spilled out of the jellium sphere is increased in PHJM. This is shown explicitly in Table II where is reported the calculated spillout

Table II. Spillout in neutral clusters with 20 atoms.

	δN	
	JM	PHJM
Li_{20}	3.3	4.3
Na_{20}	2.9	4.3
K_{20}	2.5	4.3
Rb_{20}	2.3	4.4
Cs_{20}	2.2	4.2

$$\delta N = \int_R^\infty \rho d^3r \ , \tag{30}$$

in $N = 20$ clusters.

The spillout effect is a quantum effect which can be observed through the experimental determination of the static polarizability. This point can be explicitly shown in an approximate way by approximating the electron density with the following step function:

$$\rho(r) = \rho_0 \theta(r - (R + \delta)) \ , \tag{31}$$

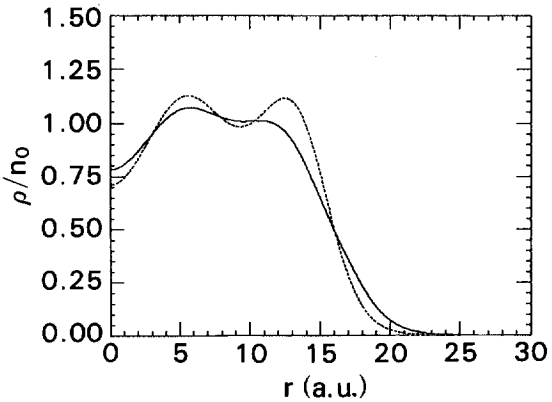

Fig. 6. Normalized density ρ/n_0 of the K_{40} cluster, calculated with JM (dashed line) and PHJM (solid line).

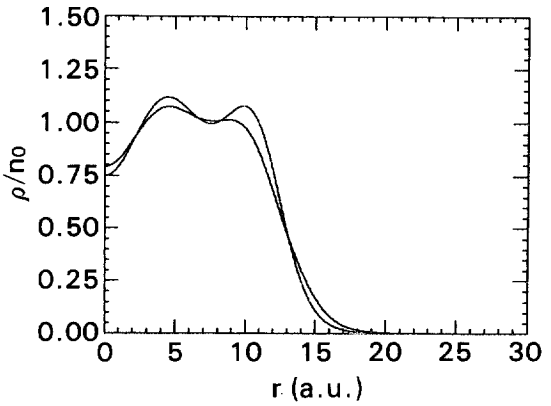

Fig. 7. Same as Fig. 6, for the Na_{40} cluster.

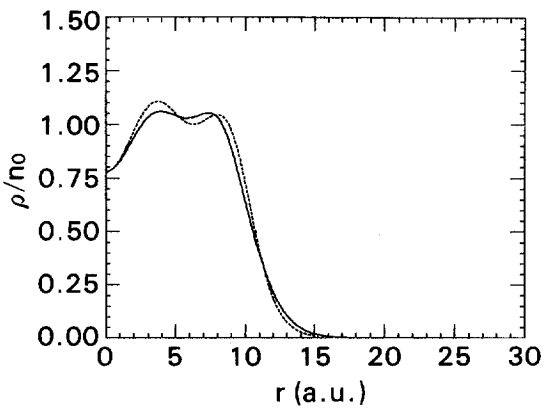

Fig. 8. Same as Fig. 6, for the Li_{40} cluster.

which in comparison with the jellium one

$$n(r) = \frac{3}{4\pi r_s^3}\theta(r-R) \ , \quad (32)$$

has a lower central density and a larger radius accounting for the spillout effect. From Eq. (30) and from the normalization condition for the densities ρ and n, in the limit $\delta N/N \ll 1$ one gets

$$\frac{\delta N}{N} = \frac{3\delta}{R} \ . \quad (33)$$

Using the result $\alpha = (R+\delta)^3$ for the polarizability associated to the density distribution (31), one finally gets

$$\alpha = R^3\left(1+\frac{\delta N}{N}\right) \ . \quad (34)$$

An increase of $\frac{\delta N}{N}$ yields then to an increase of the polarizability of the system and as a consequence to a red shift of its excitation spectrum. We then conclude that the inclusion of the ionic structure through the use of pseudohamiltonians, increases the spillout effect with respect to the jellium model and then yields to an increase of the static polarizability and to a red shift of the plasmon mode. This will be confirmed in a more quantitative way in §4.

3.3. *Ionization potentials*

The ionization potential of a cluster is the energy required to pull out one valence electron from that cluster:

$$\mathrm{IP} \equiv E(X_N) - E(X_N^+) \ , \quad (35)$$

where X_N and X_N^+ are clusters containing N ions and N or $N-1$ electrons, respectively. Ionization potentials can be measured and therefore, it is interesting to look at the model predictions. In the density functional approach, ionization potentials can be calculated by just subtracting the total energies of the initial and final clusters. In the calculations, clusters which do not correspond to a closed shell are approximated by a filling approximation. This approximation should be valid in the vicinity of a closed shell.

The early work of Lang and Kohn[17] has shown that ionization potentials in alkali metal clusters are only qualitatively described by the JM, and that inclusion of ionic structure via pseudopotentials strongly improves agreement with experiment. Recently, measurements have been done on positively charged K and Li clusters[18] up to large sizes. In Figs. 9 and 10 we compare these data to the JM and PHJM predictions. The full line on Figs. 9 and 10 is a fit to the data. For $N \to \infty$ the fit reproduces the correct value of the bulk work function W as measured in the solid. It can be seen that the JM overestimates systematically the data. This is related to the too large value of W in the bulk predicted by the JM as it was pointed out in Ref. 17). On the other hand, inclusion of ionic structure effects by the PHJM improves the ionization potential predictions and can give a quantitative agreement with experiment.

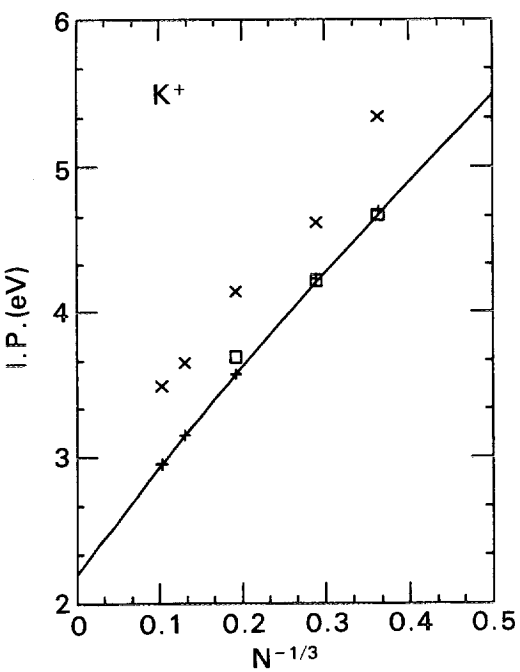

Fig. 9. Ionization potentials in K^+ clusters calculated with JM (×) and PHJM (open squares). The data points (crosses) are from Ref. 18). The solid line is a fit to the data.

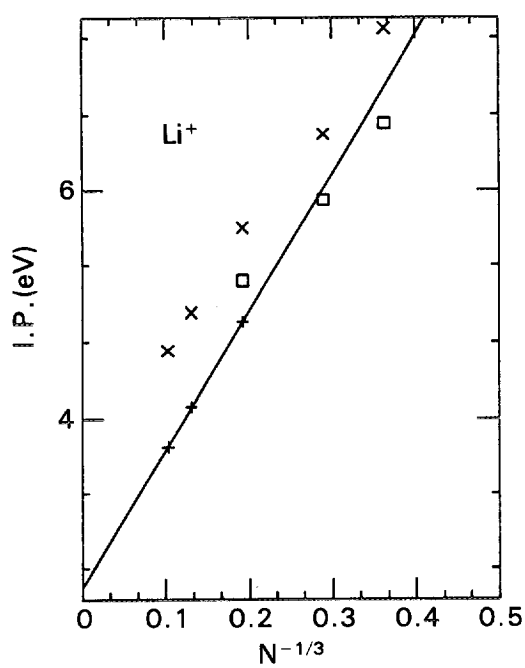

Fig. 10. Same as Fig. 9, for Li^+ clusters.

3.4. *Shells and supershells*

One possibility for identifying shell closures is to divide the total energy E into a smooth part $\bar{E}$ and a fluctuating part δE. The smooth part can be calculated by fitting E with a liquid drop expansion.[19] A shell closure will correspond to a negative peak in the shell correction energy δE . This procedure, however, requires a rather big computational effort because one must determine E for a large set of cluster sizes. The effort could be drastically reduced by replacing the total energy E with the sum of single-particle energies which are themselves calculated not self-consistently but in some Woods-Saxon potential. This method was applied by Nishioka et al.[20] to predict the magic numbers in Na clusters up to $N \simeq 4000$. The existence of supershells was also beautifully put in evidence. A more direct and self-consistent approach which was used in Ref. 21) and closely related to how magic numbers are experimentally observed, is to look at ionization potentials. A signature of major shell closure at some N is a sudden large increase of $\Delta\mathrm{IP}(N) \equiv \mathrm{IP}(N) - \mathrm{IP}(N+1)$. Let us denote by $\varepsilon_{\mathrm{HOMO}}(N)$ and $\varepsilon_{\mathrm{LUMO}}(N)$ the energies of the highest occupied and lowest unoccupied single-particle orbitals in the N-cluster, and define the quantity:

$$\Delta\varepsilon(N) \equiv \varepsilon_{\mathrm{LUMO}}(N) - \varepsilon_{\mathrm{HOMO}}(N) \ . \tag{36}$$

Apart from some rearrangement terms, $\mathrm{IP}(N)$ is approximately equal to $-\varepsilon_{\mathrm{HOMO}}(N)$ while $\mathrm{IP}(N+1)$ is approximately $-\varepsilon_{\mathrm{HOMO}}(N+1)$, i.e., close to $-\varepsilon_{\mathrm{LUMO}}(N)$. Therefore, to a good approximation one has:

$$\Delta\mathrm{IP}(N) \simeq \Delta\varepsilon(N) \ . \tag{37}$$

As an example, Fig. 11 shows the $\Delta\varepsilon(N)$ calculated for neutral Li clusters of sizes ranging from about 200 to 6000 atoms. The results are displayed by vertical bars and for a better visualization a curve is shown which corresponds to a folding of the discrete distribution with a gaussian of width 0.05 in the variable $x = N^{1/3}$. Two sequences of lines are clearly seen, one equispaced in x corresponds to major shell closures, the other one indicating subshell closures. A comparison of the folded curves obtained in JM and PHJM is shown in the upper panel of Fig. 11. Apart from some shifts in the maxima, more important for $N > 3000$, the main feature is an almost uniform scaling of the heights of the peaks. The PHJM peaks are lower than the JM ones by a factor very close to the ratio of effective masses, about 1.5. This can be related to the fact that the level spacing in a potential is inversely proportional to the effective mass.

The results of Fig. 11 can be displayed in a different way in order to exhibit supershell features. Let us take the discrete distributions of $\Delta\varepsilon(N)$ and fold them with a gaussian of width 0.10 in the variable $x = N^{1/3}$, i.e., a width larger than the distance between subshells but smaller than the distance between major shells. The resulting curves shown in Fig. 12 clearly display the beating pattern between two shell sequences usually called supershell effect. For Li clusters, one can see that the positions of the nodes obtained in JM and PHJM are somewhat different. The first node is found at $N \simeq 900$ in JM and $N \simeq 1100$ in PHJM to be compared with the experimental result of Ref. 22) indicating a node between 710 and 1065. The

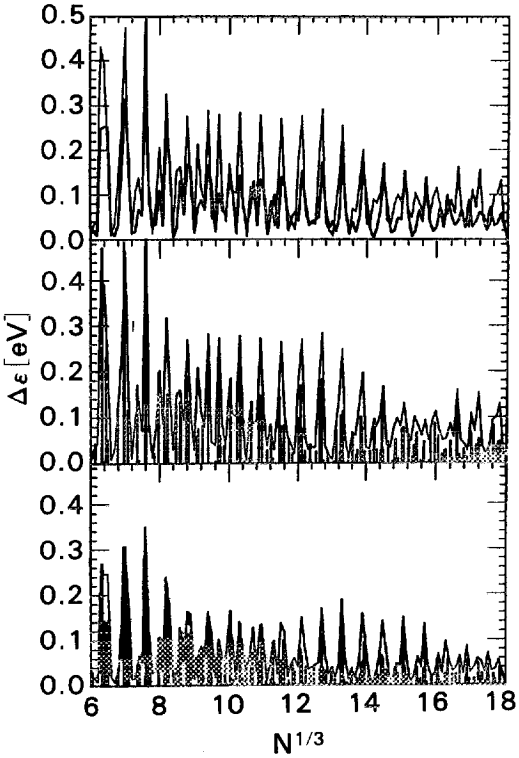

Fig. 11. $\Delta\varepsilon$ values (vertical bars) in Li clusters, as a function of $x = N^{1/3}$. The curves are obtained by folding the bars with a gaussian of width 0.05 in x and a convenient normalization. Lower panel: PHJM. Middle panel: JM. Upper panel: Comparison between JM (thin line) and PHJM (thick line).

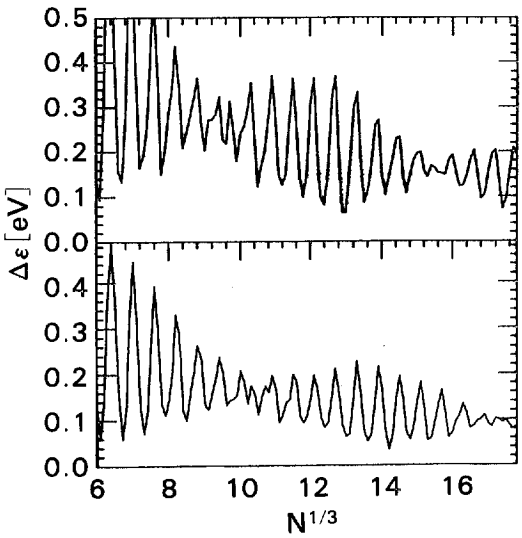

Fig. 12. $\Delta\varepsilon$ values in Li clusters, folded with a gaussian of width 0.10 in the variable $x = N^{1/3}$. Lower panel: PHJM. Upper panel: JM.

difference in the second node is more pronounced: around $N \simeq 4000$ in JM and $N \simeq 4900$ in PHJM. The origin of the shift is twofold. The geometry of the mean potential is different in the two models, and the r-dependence of the effective mass in PHJM implies that the quantization conditions for the action calculated along classical orbits are also different. Similar results are found for Na and K clusters but the shift between the two models is much smaller there.[21]

§4. Linear response and dipole plasmon

4.1. *RPA/TDLDA method*

Let us consider a general hermitian one-body operator Q :

$$Q = \int Q(\boldsymbol{r})\psi^{\dagger}(\boldsymbol{r})\psi(\boldsymbol{r})d^3r \ , \tag{38}$$

where $\psi^\dagger(\boldsymbol{r})$ and $\psi(\boldsymbol{r})$ respectively creates and annihilates an electron at point $\boldsymbol{r}$. Denoting by $|0\rangle$ and $|n\rangle$ the ground and excited states of the cluster and by ω_{n0} the corresponding excitation energies, we introduce the linear response function as:

$$\begin{aligned} R(\omega) &\equiv \sum_n |\langle 0|Q|n\rangle|^2 \left(\frac{1}{\omega_{n0}-\omega-i\eta}+\frac{1}{\omega_{n0}+\omega+i\eta}\right) \\ &= \int \sum_n \langle 0|\psi^\dagger(\boldsymbol{r})\psi(\boldsymbol{r})|n\rangle\langle n|\psi^\dagger(\boldsymbol{r}')\psi(\boldsymbol{r}')|0\rangle \\ &\quad \times \left(\frac{1}{\omega_{n0}-\omega-i\eta}+\frac{1}{\omega_{n0}+\omega+i\eta}\right) Q(\boldsymbol{r})Q(\boldsymbol{r}')d^3rd^3r' \ , \end{aligned} \tag{39}$$

where $\sum_n$ means a discrete sum over normalizable states and an integral over the continuous part of the spectrum. Clearly, the positions of the poles of $R(\omega)$ on the positive real axis give the excitation energies whereas the corresponding residues are the transition probabilities. The distribution of transition strength related to the operator Q is, for positive values of ω :

$$S(\omega) \equiv \sum_n |\langle 0|Q|n\rangle|^2 \delta(\omega-\omega_{n0}) \ = \ \frac{1}{\pi}\mathrm{Im}R(\omega) \ . \tag{40}$$

It can be shown [23] that the response function (39) can be expressed in terms of the particle-hole Green's function $G(\boldsymbol{r},\boldsymbol{r}';\omega)$. For $\omega > 0$ we have:

$$R(\omega) = \int Q(\boldsymbol{r})G(\boldsymbol{r},\boldsymbol{r}';\omega)Q(\boldsymbol{r}')d^3rd^3r' \ . \tag{41}$$

This exact expression of $R(\omega)$ is of little use as it stands because the exact many-body Green's functions obey a hierarchy of coupled equations that one cannot solve. A fruitful and widely used approximation is to truncate the chain of equations at the level of two-body (particle-hole) Green's functions so that only one-body and two-body Green's functions are involved. This is achieved by TDLDA or RPA approximations, which can be viewed as the small amplitude limit of the time-dependent Hartree-Fock (TDHF) theory. [23),24] In this limit, one can obtain an integral equation for the TDLDA or RPA Green's function $G(\boldsymbol{r},\boldsymbol{r}';\omega)$. Let us denote by H_0 the one-body Hamiltonian defined by the Kohn-Sham equations (27). The corresponding non-interacting particle-hole Green's function is:

$$\begin{aligned} G^{(0)}(\boldsymbol{r},\boldsymbol{r}';\omega) = \sum_i \phi_i^*(\boldsymbol{r}) \Big\langle \boldsymbol{r} \Big| &\frac{1}{H_0-\varepsilon_i-\omega-i\eta} \\ &+\frac{1}{H_0-\varepsilon_i+\omega-i\eta}\Big| \boldsymbol{r}'\Big\rangle \phi_i(\boldsymbol{r}') \ , \end{aligned} \tag{42}$$

where the sum is over occupied orbitals. Starting from TDHF and going over to the small amplitude limit one can show [25] that in TDLDA or RPA the interacting particle-hole Green's function $G(\boldsymbol{r},\boldsymbol{r}';\omega)$ obeys the well-known integral equation:

$$G(\boldsymbol{r},\boldsymbol{r}';\omega) = G^{(0)}(\boldsymbol{r},\boldsymbol{r}';\omega) + \int G^{(0)}(\boldsymbol{r},\boldsymbol{r}_1;\omega)V(\boldsymbol{r}_1-\boldsymbol{r}_2)G(\boldsymbol{r}_2,\boldsymbol{r}';\omega)d^3r_1d^3r_2 \ , \tag{43}$$

where the effective particle-hole residual interaction is the functional derivative of that part of the Kohn-Sham Hamiltonian (27) which depends on the electronic density:

$$V(\boldsymbol{r}_1 - \boldsymbol{r}_2) = \frac{\delta W}{\delta \rho}(\boldsymbol{r}_1, \boldsymbol{r}_2) \;=\; \frac{1}{|\boldsymbol{r}_1 - \boldsymbol{r}_2|} + \frac{\delta^2 E_{xc}}{\delta \rho^2}\delta(\boldsymbol{r}_1 - \boldsymbol{r}_2)\ . \tag{44}$$

Assuming spherical symmetry, all quantities $G^{(0)}$, G and V can be expanded in multipole series like in (22) and the multidimensional equation (43) becomes a set of one-dimensional equations where different multipoles are uncoupled:

$$G_L(r, r'; \omega) = G_L^{(0)}(r, r'; \omega) + \int G_L^{(0)}(r, r_1; \omega) V_L(r_1, r_2) G_L(r_2, r'; \omega) r_1^2 r_2^2 dr_1 dr_2. \tag{45}$$

The last step is to construct explicitly the non-interacting Green's function $G^{(0)}$:

$$G^{(0)}(\boldsymbol{r}, \boldsymbol{r}'; \omega) = \sum_i \sum_m \phi_i^*(\boldsymbol{r})\phi_m(\boldsymbol{r}) \left[\frac{1}{\varepsilon_m - \varepsilon_i - \omega - i\eta} + \frac{1}{\varepsilon_m - \varepsilon_i + \omega - i\eta} \right] \phi_m^*(\boldsymbol{r}')\phi_i(\boldsymbol{r}')\ , \tag{46}$$

where $\sum_m$ in principle includes a continuous sum over unbound states but occupied states are excluded from this summation. This restriction, which avoids Pauli principle violation, comes from the cancellation of all hole-hole contributions in the first and second term of (42). Then, one can solve the Kohn-Sham equations (27) using the self-consistent potential W and imposing a box boundary condition in order to discretize the single-particle continuum, and the discrete sums over i and m in (46) can be performed explicitly if one chooses a cut-off on the number of states m that one wants to include. Alternatively, one may choose to transform the integral equation (45) into a matrix equation in particle-hole configuration space and diagonalize the RPA secular matrix.[24] If one is interested in studying the effects of the single-particle continuum, one can also start from expression (42) and use an exact representation of the single-particle Green's functions. Let us expand into multipoles the single-particle Green's function $\langle \boldsymbol{r} \frac{1}{H_0 - z_i - i\eta} | \boldsymbol{r}' \rangle$ where $z_i = \varepsilon_i \pm \omega$:

$$\left\langle \boldsymbol{r} \left| \frac{1}{H_0 - z_i - i\eta} \right| \boldsymbol{r}' \right\rangle = \frac{1}{rr'} \sum_{lm} Y_{lm}^*(\hat{r}) g_l(r, r'; z_i) Y_{lm}(\hat{r}')\ . \tag{47}$$

The function $g_l(r, r'; z_i)$ is the resolvent of the radial part of H_0 for the l-partial wave, i.e., of a second order differential operator. Hence, this resolvent can be expressed in terms of two linearly independent eigenfunctions, u and w , corresponding to the eigenvalue z_i.[26] These eigenfunctions must satisfy the following boundary conditions: a) at origin, u is regular and behaves like r^{l+1} whereas w is irregular and goes like r^{-l}; b) at infinity, and for positive values of z_i, $u(r)$ behaves like a standing wave whereas $w(r)$ has a radially outgoing behavior. If z_i is negative, $u(r)$ is exponentially increasing and $w(r)$ is exponentially decreasing, asymptotically. Then, the

closed form expression of g_l is:

$$g_l(r,r';z_i) = \frac{2m^*}{W(w,u)} u(r_<)w(r_>) \ , \tag{48}$$

where $W(w,u)$ is the Wronskian of the two eigenfunctions, $r_<$ and $r_>$ are respectively the smaller and the larger of r and r'. The quantity $m^*(r)/W(w,u)$ is independent of r .

4.2. *Response function results*

We first illustrate the RPA/TDLDA method by looking at some typical cases and comparing the predictions of the various jellium models (JM, PHJM, PPJM) with experimental data obtained in measurements of the optical response of clusters. If one chooses the dipole operator $Q = z$ for calculating the response function (39) then the dipole transition strength $S(\omega)$ of Eq. (40) is simply related to the photoabsorption cross-section $\sigma(\omega)$ by:

$$\sigma(\omega) = \frac{4\pi^2}{c} \omega S(\omega) \ , \tag{49}$$

whereas the dipole polarizability α is given by

$$\alpha = \mathrm{Re}\ R(\omega)|_{\omega=0} \ . \tag{50}$$

It is also customary to discuss dipole strength distributions in terms of the energy-weighted sum rule (EWSR) or f-sum rule:

$$\begin{aligned} M_1 &\equiv \sum_n |\langle 0|Q|n\rangle|^2 \omega_{n0} \\ &= \int S(\omega)\omega d\omega \ . \end{aligned} \tag{51}$$

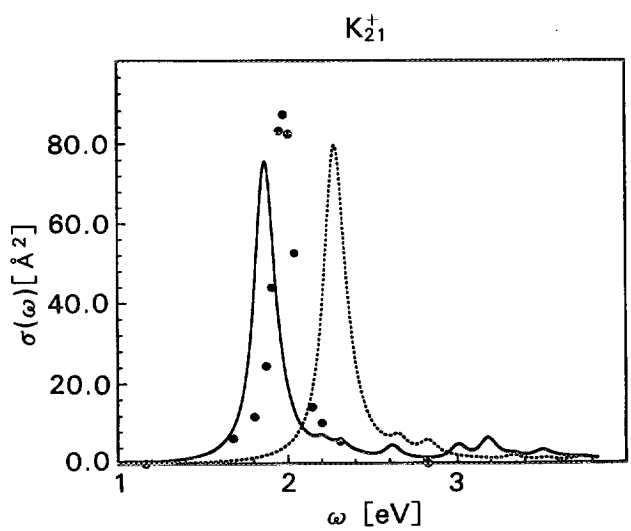

Fig. 13. Photoabsorption cross-sections in K^+_{21} calculated with JM (dashed line) and PHJM (solid line). Data points are from Ref. 28).

In Fig. 13 are shown photoabsorption cross-sections calculated in JM and PHJM [27] and compared to data from Bréchignac et al. [28] for the ionized cluster K_{21}^+. It can be seen that the models both predict a collective dipole plasmon but the JM plasmon energy is higher than the experimental one. Because of its effective mass the PHJM red-shifts the plasmon and brings it to a better agreement with experiment.

In Fig. 14 are shown dipole strength distributions in the neutral cluster Na_{20} calculated with the three jellium models (JM, PHJM, PPJM). [9] They are compared with data from Ref. 29). The collectivity of the plasmon is weaker in the JM than in the other models and its energy is higher. The more sophisticated models (PHJM and PPJM) clearly improve agreement with experiment.

The case of Li_{139}^+ is shown in Fig. 15 where the calculations are from Ref. 9) and the data from Ref. 30). In Li clusters one expects a large difference between JM and PHJM because the latter has a large effective mass ($m^* \sim 1.5$). This indeed produces a red shift of about 1 eV and brings the plasmon close to the experimental

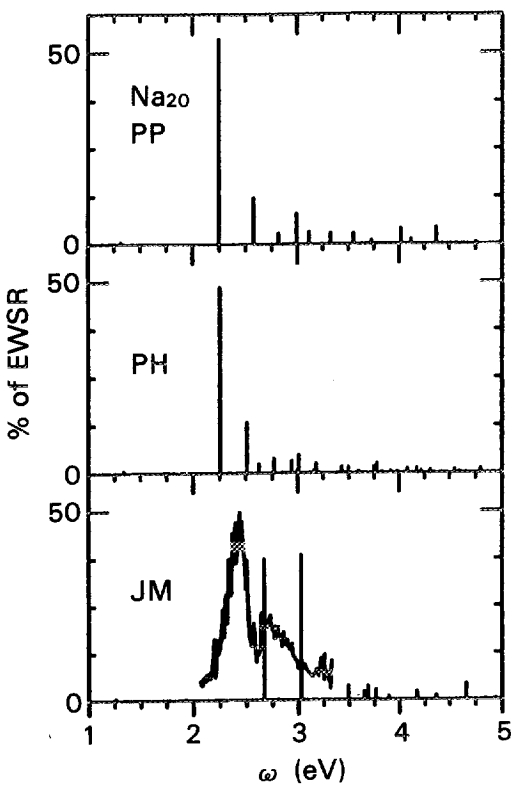

Fig. 14. Dipole strength distributions (in percentage of EWSR) in Na_{20} calculated with JM (lower panel), PHJM (middle panel) and PPJM (upper panel). Data shown in lower panel are from Ref. 29), in arbitrary scale.

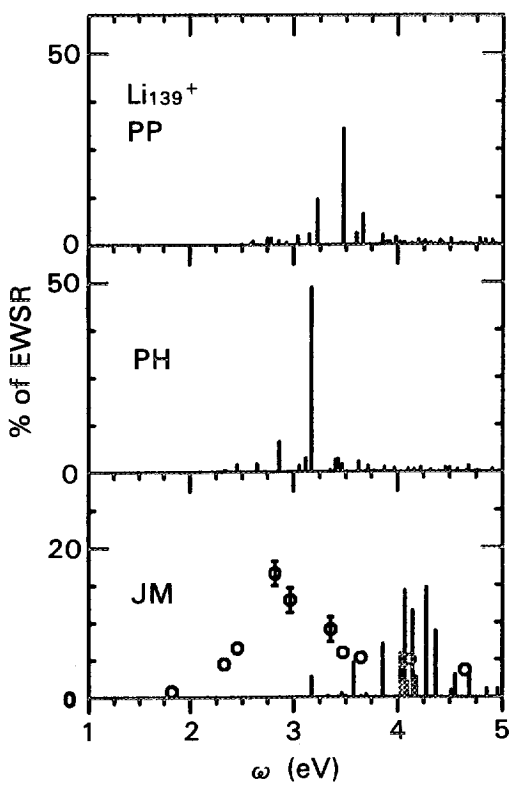

Fig. 15. Same as Fig. 14, for Li_{139}^+. Data points from Ref. 30), in arbitrary scale.

peak. The more complete calculation of PPJM produces a more moderate shift but it is clear that ionic structure effects are still important.

4.3. *Sum rules and spillout effect*

The plasmon energy can be discussed in general terms if one makes use of two sum rules which are easily calculable in RPA/TDLDA, namely the $M1$ sum rule of Eq. (51) and the cubic energy-weighted sum rule M_3:

$$M_3 \equiv \sum_n |\langle n|Q|n\rangle|^2 \omega_{n0}^3 = \int S(\omega)\omega^3 d\omega \ . \tag{52}$$

The energy ω_3 defined as:

$$\omega_3 \equiv \left(\frac{M_3}{M_1}\right)^{1/2} , \tag{53}$$

can represent a good estimate of the plasmon energy when a large fraction of strength is exhausted by the collective plasmon, as it is generally the case.

The exact values of M_1 and M_3 evaluated with the exact eigenstates of the system satisfy the following identities:

$$M_1 = \frac{1}{2}\langle 0|[Q,[H_{el},Q]]|0\rangle,$$
$$M_3 = \frac{1}{2}\langle 0|[[Q,H_{el}],[H_{el},[H_{el},Q]]]|0\rangle \ . \tag{54}$$

It can be shown that the expectation values of the above commutators on the Kohn-Sham ground state are equivalent to evaluating the expressions (51) and (52) with RPA energies and matrix elements.

Let us first evaluate M_1 in the case of JM. For H_{el} we must take the Hamiltonian (3) with the last term replaced by $H_{e\text{-}i}$ of (6) or (20). Using the dipole operator $Q = z$ one has:

$$[H_{el},Q] = -\frac{1}{2}\sum_{i=1}^{N} \nabla_z^{(i)} \ , \tag{55}$$

and hence the well-known Thomas-Reiche-Kuhn (TRK) sum rule:

$$M_1 = \frac{N}{2m} \ . \tag{56}$$

To evaluate M_3 we rewrite (54) as:

$$M_3 = \frac{\partial^2}{\partial \nu^2}\langle \nu|H_{el}|\nu\rangle|_{\nu=0} \tag{57}$$

with $|\nu\rangle$ being the scaled state:

$$|\nu\rangle = e^{\nu[H_{el},Q]}|0\rangle \ . \tag{58}$$

In the JM case where (55) holds $|\nu\rangle$ describes a translation of the valence electrons as a whole. The sum rule M_3 can then be regarded as the restoring force associated with this translation and the energy ω_3 as the energy of this collective motion. In calculating (57) only $\langle\nu|H_{e\text{-}i}(\boldsymbol{r})|\nu\rangle$ can contribute, and one simply gets:

$$\begin{aligned} M_3 &= \frac{1}{2m}\int \rho(\boldsymbol{r})\nabla_z^2 H_{e\text{-}i}(\boldsymbol{r})d^3r \\ &= \frac{2\pi}{3m}\int \rho(\boldsymbol{r})n(\boldsymbol{r})d^3r \ , \end{aligned} \tag{59}$$

where the second line of (59) is obtained by making use of the Poisson equation: $\nabla^2 H_{e\text{-}i}(\boldsymbol{r}) = 4\pi n(\boldsymbol{r})$. Defining the number of electrons inside the jellium sphere of radius $R = r_s N^{1/3}$ by:

$$N_{\text{ins}} = \int_{r\le R} \rho(\boldsymbol{r})d^3r \ , \tag{60}$$

we can write:

$$M_3 = \frac{1}{2}\omega_{\text{Mie}}^2 N_{\text{ins}} \ , \tag{61}$$

where $\omega_{\text{Mie}} = r_s^{-3/2}$ is the classical Mie frequency [31] of a spherical conductor, in a.u. Combining the above results we finally get, in the JM case:

$$\omega_3 = \omega_{\text{Mie}}\left(\frac{N_{\text{ins}}}{N}\right)^{1/2} \ . \tag{62}$$

The so-called spillout effect, i.e., the fact that part of the electrons are leaking out of the jellium sphere ($N_{\text{ins}} < N$) leads to a lowering of the plasmon frequency as compared to the classical Mie value.

Let us now turn to the PHJM case. To evaluate M_1 one must use H_{el} of Eq. (3) with the last term replaced by $\hat{V}_I$ of (23). The expectation value of the double commutator now becomes:

$$\begin{aligned} M_1 &= \frac{1}{2m}\int \left[1 + \alpha(\boldsymbol{r}) + \frac{4}{3}r^2\beta(\boldsymbol{r})\right]\rho(\boldsymbol{r})d^3r \\ &\simeq \frac{N}{2m}\left(\frac{m}{m^*(r=0)}\right) \ , \end{aligned} \tag{63}$$

if we neglect $\beta(\boldsymbol{r})$ which is always small and approximate $m^*(\boldsymbol{r})$ by $m^*(0)$. For M_3 we can look for an approximate analytical expression by dropping again $\beta(\boldsymbol{r})$ and replacing $m^*(\boldsymbol{r})$ by $m^*(0)$. Then,

$$|\nu\rangle \simeq \exp\left(-\frac{\nu}{2}\frac{m}{m^*(0)}\sum_i \nabla_z^{(i)}\right)|0\rangle \tag{64}$$

and

$$M_3 \simeq \frac{1}{2m}\left(\frac{m}{m^*(0)}\right)^2 \int \rho(\boldsymbol{r})\nabla_z^2 U_I(\boldsymbol{r})d^3r \ , \tag{65}$$

where $U_I(\boldsymbol{r})$ is defined in (24). For very large size clusters the function $\nabla_z^2 U_I(\boldsymbol{r})$ tends to $\frac{4\pi}{3}n(\boldsymbol{r})$ and the integral in (65) is proportional to $N_{\rm ins}$. In this limit we finally obtain, in the PHJM case:

$$\omega_3 \simeq \omega_{\rm Mie}\left(\frac{N_{\rm ins}}{N}\right)^{1/2}\left(\frac{m}{m^*(0)}\right)^{1/2} . \tag{66}$$

In clusters like Li where $m^*(0)$ is somewhat larger than m one can expect, in addition to the spillout lowering effect, another source of redshift of the plasmon frequency due to ionic structure effects via the effective mass.

4.4. *Systematics of dipole plasmon energies*

In Ref. 21) extensive calculations of dipole plasmons in alkali metal clusters using both JM and PHJM have been performed in TDLDA. The range of large size clusters (up to $N \simeq 5500$) has been explored. In Table III their results are summarized.

Table III. Peak energies $\omega_{\rm peak}$ and ω_3-energies (in eV) of dipole plasmons in large alkali metal clusters, calculated in TDLDA. Percentages of EWSR exhausted by the collective plasmon are also shown (from Ref. 21)).

	JM				PHJM		
N	$\omega_{\rm peak}$	ω_3	% EWSR	N	$\omega_{\rm peak}$	ω_3	% EWSR
Li							
1502	4.45	4.51	70	1314	3.49	3.55	60
2654	4.54	4.53	89	2048	3.57	3.58	66
3028	4.55	4.53	88	3050	3.64	3.60	87
4074	4.56	4.54	88	4154	3.65	3.62	89
5470	4.57	4.55	90	5500	3.66	3.63	90
Na							
1314	3.36	3.38	62	1314	3.20	3.20	55
1502	3.38	3.39	70	2048	3.22	3.23	63
2654	3.41	3.41	75	3028	3.25	3.26	68
4074	3.44	3.42	88	4154	3.29	3.27	78
5470	3.45	3.43	92	5470	3.30	3.29	76
K							
912	2.45	2.48	88	832	2.24	2.33	60
2018	2.49	2.49	93	2018	2.40	2.39	82
2998	2.51	2.50	90	3028	2.44	2.41	88
3848	2.52	2.50	96	3848	2.46	2.42	90
5568	2.53	2.51	94	5108	2.49	2.43	91

A considerable lowering of plasmon frequencies in the PHJM case can be seen, especially in Li clusters. On the basis of expressions (62) and (66) the N-dependence of ω_3 was extracted by parameterizing the spillout in the form:

$$\left(\frac{N_{\rm ins}}{N}\right)^{1/2} = 1 + cN^{-1/3} . \tag{67}$$

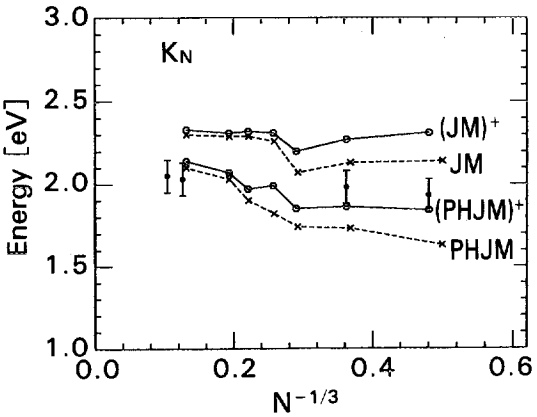

Fig. 16. Peak energies of photoabsorption cross-sections in K_N (crosses) and K_N^+ (open circles) clusters. The two upper curves are calculated with JM, the two lower ones with PHJM. Data points from Ref. 28) correspond to K_N^+ clusters.

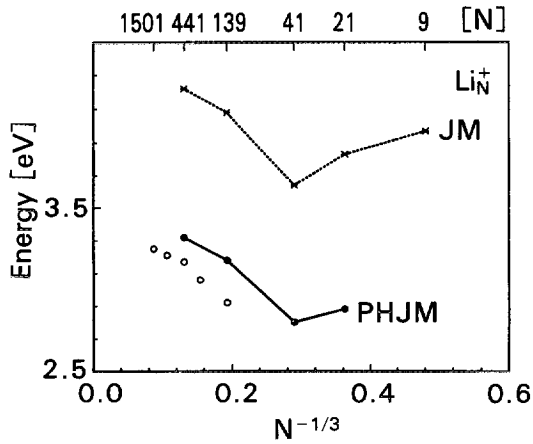

Fig. 17. Peak energies of photoabsorption cross-sections in Li_N^+ clusters calculated with JM (crosses) and PHJM (dots). Data points (open circles) from Ref. 30).

The deduced values of c and the infinite size limit ($N \to \infty$) of ω_3 are reported in Table IV.

Table IV. Slope parameters c and $\omega_3(\infty)$ limit (in eV) giving the N-dependence of dipole plasmon energies in alkali metal clusters (from Ref. 21)).

Cluster	Model	c	$\omega_3(\infty)$
Li	JM	-0.28	4.62
	PHJM	-0.60	3.76
Na	JM	-0.33	3.49
	PHJM	-0.73	3.43
K	JM	-0.23	2.54
	PHJM	-0.87	2.56

In all three types of alkali clusters the slope is much larger in absolute value for PHJM than for JM. This fact is related to the larger diffusivity of electronic densities in PHJM and it explains how, in the case of K clusters, the peak energies for finite sizes are larger in JM but the infinite limit is higher in PHJM. Experimentally, a value of 3.55 eV for ω_{peak} extrapolated to $N \to \infty$ in Li clusters is reported in Ref. 30). Going from JM to PHJM, the corresponding calculated values of $\omega_3(\infty)$ come down from 4.62 eV to 3.76 eV. The change is less marked in Na and K clusters.

In Fig. 16 one can see a comparison of plasmon peak energies calculated[27] in some medium-size K clusters (neutral and ionized) together with peak energies measured in ionized K clusters.[28] In Fig. 17 is shown a similar comparison for ionized Li clusters with the calculated results of Ref. 12) and the data of Ref. 30). In both cases of K and Li clusters there is a distinct improvement towards better agreement with experiment when PHJM is used.

4.5. *Static dipole polarizability*

Let us consider a cluster governed by the Hamiltonian H_{el} and submitted to a

dipole constraint λz, and let us denote by $|\lambda\rangle$ the solution of the variational problem:

$$\delta\langle\lambda|H_{el} - \lambda z|\lambda\rangle = 0 \ . \tag{68}$$

The static dipole polarizability is defined as:

$$\alpha \equiv \frac{\partial\langle\lambda|z|\lambda\rangle}{\partial\lambda}\Big|_{\lambda=0} \ . \tag{69}$$

It is easy to calculate α in the classical case of a metal sphere of radius R with ionic density $n(r)$ (constant for $r \leq R$ and zero for $r > R$) and electronic density $\rho(r)$. Its classical energy is:

$$E = \frac{1}{2}\int \frac{[\rho(\boldsymbol{r}) - n(\boldsymbol{r})][\rho(\boldsymbol{r}') - n(\boldsymbol{r}')]}{|\boldsymbol{r} - \boldsymbol{r}'|} d^3r d^3r' \ . \tag{70}$$

The variational problem:

$$\delta\left\{E - \lambda\int z[\rho(\boldsymbol{r}) - n(\boldsymbol{r})]d^3r\right\} = 0 \tag{71}$$

has the solution:

$$\delta\rho(\boldsymbol{r}) = \lambda\frac{3}{4\pi}\frac{z}{r}\delta(r - R) \ , \tag{72}$$

from which we find:

$$\begin{aligned}\alpha &= \frac{1}{\lambda}\int z\delta\rho(\boldsymbol{r})d^3r \\ &= R^3 \ .\end{aligned} \tag{73}$$

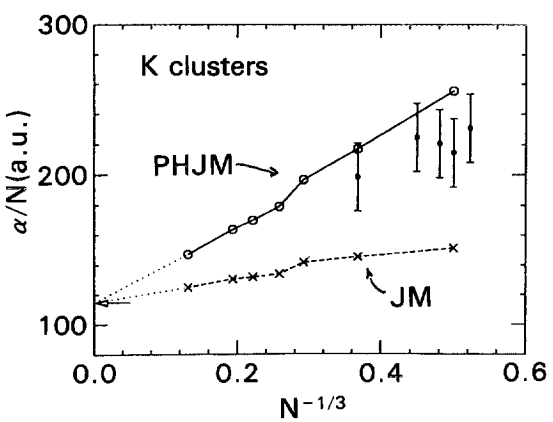

Fig. 18. Static polarizability per particle of K_N clusters calculated with JM (crosses) and PHJM (open circles). Data points are from Ref. 2). The arrow on vertical scale shows the bulk limit value, r_s^3.

In the quantum mechanical case the polarizability α, which is twice the inverse energy-weighted sum rule, can be calculated from the response function at zero excitation energy (see Eq. (50)). This was done by Serra et al.[27] for the case of closed-shell neutral K clusters for the sizes from $N = 8$ to $N = 440$. The results are shown in Fig. 18 together with measurements[2] done on small size clusters ($N = 7, 8, 9, 11$ and 20). It can be seen that both JM and PHJM extrapolate to the same bulk limit of polarizability per particle, $(\alpha/N)_{\text{bulk}} = r_s^3$. However, for finite size the PHJM predicts a larger enhancement of α/N.

The slopes of the calculated results can be related to the increase δ of the effective cluster radius (see Eq. (34)):

$$\alpha = (R+\delta)^3 \simeq R^3 \left(1 + \frac{3\delta}{r_s}\frac{1}{N^{1/3}} + \cdots\right) . \tag{74}$$

From Fig. 18 one has $\delta = 3.2$ for PHJM and $\delta = 1.1$ for JM. In the limit of large clusters the value of δ coincides with the centroid of the induced charge relative to the cluster edge[32] and hence with the centroid of induced charge for a flat surface. This distance was calculated for a plane by Lang and Kohn[33] in the JM. They found $\delta = 1.3 \pm 0.2$ for $r_s = 4$ and $\delta = 1.2 \pm 0.2$ for $r_s = 6$. The value $\delta = 1.1$ of Ref. 27) was obtained with $r_s = 4.86$ and it agrees well with Ref. 33). The ionic core effects present in PHJM are responsible for a significant increase of δ over the JM value.

From Fig. 18 it can be seen that the PHJM result for K_{20} is compatible with experiment while the JM prediction is too low. For sizes smaller than $N = 20$ the jellium assumption might be questionable.

§5. Correlations in clusters

5.1. *The RPA ground state*

The density functional approach is based on an energy density functional which is designed to give the best approximation to the ground state energy. However, the corresponding wave function, the Kohn-Sham Slater determinant, is just an uncorrelated wave function which does not necessarily describe correctly the ground state wave function. In this section, we address the question of how correlated is the cluster ground state when we compare it to the Kohn-Sham determinant $|\mathrm{KS}\rangle$ as a reference state.

A first hint that correlations are probably important is provided by the extreme case of very highly ionized clusters. The example of Na_{60}^{20+} (60 atoms, 40 valence electrons) was considered by Yannouleas et al.[34] Although such clusters are unstable against spontaneous fission (the ratio $f = x^2/N$ of the square of excess charge by the number of atoms is far above the critical value $f_{\mathrm{cr}} = 0.39$ for sodium clusters as given by a liquid-drop estimate[35]) they are interesting because they represent an exact many-body limit where the plasmon frequency is known. Indeed, the confining potential generated by the positive background can be well approximated by its harmonic part. Then, the center-of-mass motion of the electron gas separates exactly from the individual motions, and the photoabsorption spectrum must consist of one line having 100 % of the oscillator strength, at the frequency of the confining parabolic potential.[36),37] This potential is:

$$\begin{aligned} U(r) &= \mathrm{const} + \frac{2\pi n_0}{3} r^2 \\ &= \mathrm{const} + \frac{1}{2} m\omega_{\mathrm{Mie}}^2 r^2 , \end{aligned} \tag{75}$$

where $n_0 = (4\pi r_s^3/3)^{-1}$ is the jellium density. Thus, the plasmon frequency coincides with the classical Mie frequency which is 3.4 eV for sodium clusters.

If the ground state is assumed to be $|\mathrm{KS}\rangle$, dipole plasmon modes are just superposition of 1particle-1hole ($1p$-$1h$) configurations which can be calculated in Tamm-Dancoff approximation (TDA). The corresponding result which is shown in the upper part of Fig. 19 consists of several separate states. On the other hand, the RPA result (lower part of Fig. 19) shows a single state at 3.14 eV exhausting practically all the dipole strength. This example shows firstly that RPA/TDLDA is appropriate for describing correctly the excitation spectrum of the cluster or at least its dipole part, and secondly that the RPA ground state, $|\mathrm{RPA}\rangle$ must be somewhat different from the uncorrelated state $|\mathrm{KS}\rangle$.

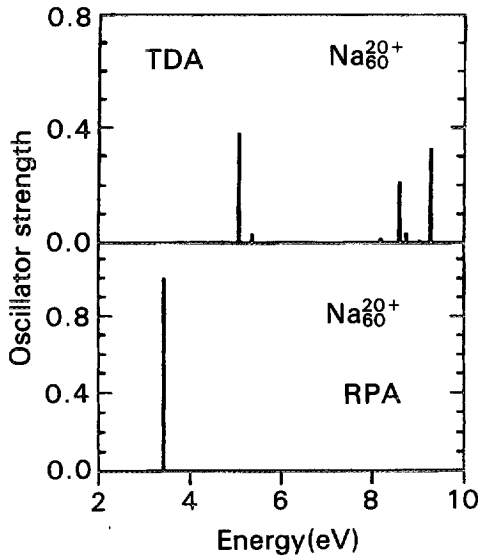

Fig. 19. TDA and RPA oscillator-strength distributions of the dipole mode in the highly ionized Na_{60}^{20+} cluster, calculated with the JM model.

The difference between $|\mathrm{RPA}\rangle$ and $|\mathrm{KS}\rangle$ has been studied quantitatively by Yannouleas et al.[34] for Na clusters of various sizes. Let us briefly review their results. Denoting by $a^\dagger_{lm\sigma}$ the creation operator of an electron in a delocalized state with orbital angular momentum (l, m) and spin z-component σ and using subscripts p, h to indicate unoccupied and occupied states, respectively, the angular-momentum coupled particle-hole operators are:

$$A^\dagger_{ph}(LM) \equiv \frac{1}{\sqrt{2}} \sum_{m_p, m_h} (l_p l_h m_p m_h | LM)(-1)^{l_h + m_h} a^\dagger_{l_p m_p \sigma} a_{l_p - m_h \sigma} \ . \tag{76}$$

In RPA, excited states $|\nu\rangle$ are of the form:

$$\begin{aligned} |\nu\rangle &= O^\dagger_\nu |\mathrm{RPA}\rangle \ , \\ O^\dagger_\nu &= \sum_{ph} X^{(\nu)}_{ph} A^\dagger_{ph} - Y^{(\nu)}_{ph} A_{ph} \ , \end{aligned} \tag{77}$$

where the RPA ground state $|\mathrm{RPA}\rangle$ is the vacuum for the ν-excitations:

$$O_\nu |\mathrm{RPA}\rangle = 0 \ . \tag{78}$$

The condition (78) together with the quasi-boson approximation:

$$[A_{ph}(LM), A^\dagger_{p'h'}(L'M')] \simeq \delta_{pp'} \delta_{hh'} \delta_{LL'} \delta_{MM'} \ , \tag{79}$$

allow one to build the RPA secular equations whose solutions are the eigenvector amplitudes $(X^{(\nu)}_{ph}, Y^{(\nu)}_{ph})$ and eigenvalues ω_ν. Then, the ground state $|\mathrm{RPA}\rangle$ has the

exponential form:[38),39)]

$$|\mathrm{RPA}\rangle = N_0 \exp\left\{-\frac{1}{2}\sum_{LM}\sum_{\substack{ph\\p'h'}}(-1)^{L-M}C^{(L)}_{php'h'} \times A^{\dagger}_{ph}(LM)A_{p'h'}(L-M)\right\}|\mathrm{KS}\rangle\ , \tag{80}$$

where the correlation coefficients $C^{(L)}_{php'h'}$ are solutions of the set of equations:

$$\sum_{ph} X^{(\nu)}_{ph}(L)C^{(L)}_{php'h'} = Y^{(\nu)}_{p'h'}(L)\ . \tag{81}$$

The probability P_{2n} to find $2np$-$2nh$ configurations in $|\mathrm{RPA}\rangle$ is found by looking at the expansion of the scalar product $\langle\mathrm{RPA}|\mathrm{RPA}\rangle$:

$$P_{2n} = N_0^2\frac{1}{n!}\left(\frac{u^2}{2}\right)^n\ , \tag{82}$$

where

$$N_0^2 = \exp\left(-\frac{u^2}{2}\right) \tag{83}$$

and

$$u^2 = \sum_L\sum_{ph,p'h'}(2L+1)\left(C^{(L)}_{php'h'}\right)^2\ . \tag{84}$$

In particular, $P_0 = N_0^2$ is the probability for finding the uncorrelated state $|\mathrm{KS}\rangle$ in the correlated ground state $|\mathrm{RPA}\rangle$. Figure 20 shows the values of P_{2n} for Na clusters of various sizes.[34)] It can be seen that for large enough clusters, $|\mathrm{KS}\rangle$ is practically orthogonal to $|\mathrm{RPA}\rangle$ and that on the average more than 5% of the electrons are excited outside the Kohn-Sham core. The RPA ground state is highly correlated and contains a large number of particle-hole pairs.

This result is at first sight intriguing and one might suspect that the quasi-boson approximation (79) could be strongly violated and that RPA itself could be invalidated. Indeed, one must check the expectation value of the commutator (79):

$$\langle\mathrm{RPA}|[A_{ph}(LM), A^{\dagger}_{p'h'}(LM)]|\mathrm{RPA}\rangle = \delta_{pp'}\delta_{hh'}(N_h - N_p)\ , \tag{85}$$

where N_p and $1 - N_h$ are the occupation number of an unoccupied state and the depletion number of an occupied state, respectively. These numbers can be calculated according to:

$$\begin{aligned} N_p &\equiv \langle\mathrm{RPA}|a^{\dagger}_p a_p|\mathrm{RPA}\rangle \\ &= \frac{1}{2}\sum_{L\nu h}\frac{2L+1}{2(2l_p+1)}\left(Y^{(\nu)}_{ph}(L)\right)^2 \end{aligned} \tag{86}$$

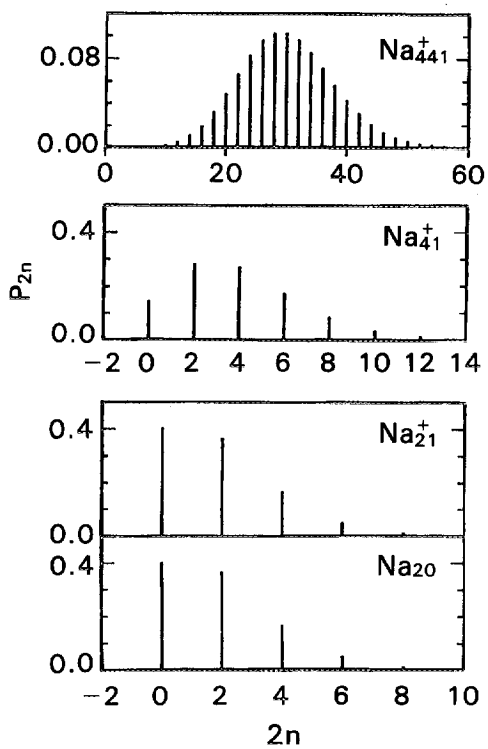

Fig. 20. Probability distributions P_{2n} in Na_{20}, Na^+_{21}, Na^+_{41} and Na^+_{441} clusters, calculated with JM model.

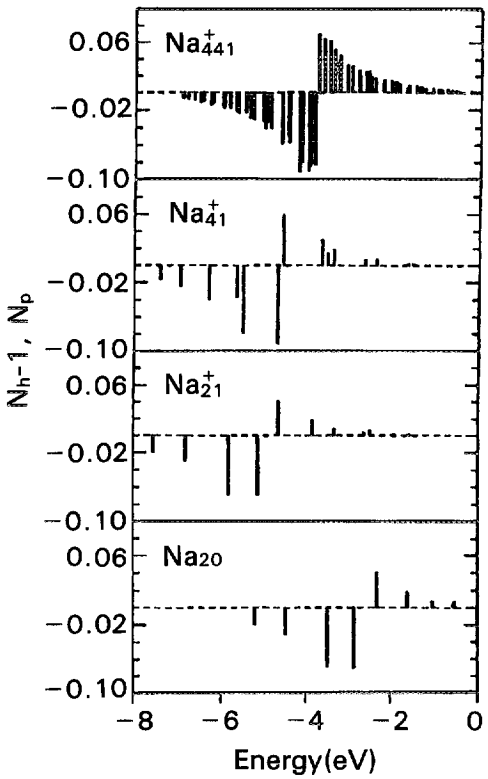

Fig. 21. Occupation numbers $N_p > 0$ for unoccupied states, and the opposite of depletion numbers $N_h - 1 < 0$ for occupied states, in Na_{20}, Na^+_{21}, Na^+_{41} andNa^+_{441} clusters.

and

$$1 - N_h \equiv \langle \mathrm{RPA} | a_h a_h^\dagger | \mathrm{RPA} \rangle = \frac{1}{2} \sum_{L\nu p} \frac{2L+1}{2(2l_h+1)} \left(Y_{ph}^{(\nu)}(L) \right)^2 . \tag{87}$$

In Fig. 21 are shown the value of N_p and $1 - N_h$ calculated by Yannouleas et al.[34] They are always small and never exceed 0.10, thus justifying the quasi-boson assumption (79) as far as expectation values are concerned.

5.2. *Physical origin of strong ground-state correlations*

The strong correlation in clusters is a manifestation of the long range character of the Coulomb force. A consequence of the long range of the force is that the plasmon energy, as a function of the size, slowly increases and approaches a finite value, the classical Mie energy. Note that this is in contrast with the behavior of giant resonance energies in atomic nuclei, which decrease as $A^{-1/3}$. In clusters, the finite value of the Mie energy results in large values of the backward amplitudes

Y as compared to the forward amplitudes X and thus to enhanced ground state correlations, according to Eqs. (80) and (81).

The above ideas can be better illustrated by a schematic example. Let us consider the dipole mode and assume that it has one collective plasmon $|c\rangle$ exhausting all the strength (see, e.g., the example of Fig. 19). Using a separable approximation for the Coulomb force[40] the X and Y amplitudes are given by:

$$X_{ph}^{(c)} = C\frac{\langle p\|z\|h\rangle}{\omega_c - \varepsilon_{ph}},$$
$$Y_{ph}^{(c)} = C\frac{\langle p\|z\|h\rangle}{\omega_c + \varepsilon_{ph}}, \tag{88}$$

where $\varepsilon_{ph} = \varepsilon_p - \varepsilon_h$ is the unperturbed particle-hole energy and the numerator is the reduced matrix element of the dipole operator, C being a normalization constant. Thus, the ratio of amplitudes for a given configuration is:

$$\frac{Y_{ph}^{(c)}}{X_{ph}^{(c)}} = \frac{\omega_c - \varepsilon_{ph}}{\omega_c + \varepsilon_{ph}}. \tag{89}$$

The main particle-hole transitions contributing to the TRK sum rule are those corresponding to one or three major shell jumps. Their energies vary as $N^{-1/3}$ and become negligible compared to ω_c in large systems where ω_c tends to ω_{Mie}. Thus, backward amplitudes become comparable in size to forward amplitudes and this is the origin of the large correlation coefficients $C_{php'h'}$ (see Eq. (81)). The above schematic example is supported by examining the results of detailed calculations. For instance, in Refs. 41) and 42) it is found that the largest $Y_{ph}^{(c)}/X_{ph}^{(c)}$ ratios are 0.30 in Na_8, 0.57 in Na_{60}^{20+}, 0.73 in Na_{338}, 0.81 in Na_{952} and 0.85 in Na_{1982}.

5.3. *Anharmonicities in two-plasmon spectra*

The strong ground state correlations are a distinct feature of atomic clusters which is in contrast with other Fermionic systems like atomic nuclei. Another marked difference between them is exhibited in the behavior of their respective multi-excitation spectra. In nuclei there are many experimentally known cases of harmonic spectra for multi-excitations. To name just one recent example, it has been observed in Coulomb excitation experiments induced by fast heavy ion beams[43] that the well-known giant dipole resonance (GDR) as well as the double GDR can be both excited and that the energy of the double GDR is very close to twice the energy of the GDR, with a total width nearly equal to $\sqrt{2}$ times that of the GDR. Thus, nuclear spectra possess components of multiphonon type with rather small anharmonicity effects. It is interesting to see whether such a situation exists in clusters and if one can expect a multi-plasmon spectrum with harmonic energy spacing. This question has been examined by Catara et al.[44] and we shall briefly outline their study here.

One starts from a Hamiltonian H which is the sum of two terms, a one-body Hamiltonian H_0 which can be thought of as the one corresponding to the Kohn-Sham mean field, and a residual two-body interaction V which is just the Coulomb force

between valence electrons. The Hamiltonian H_0 defines the single-particle occupied states, h and p. One can build the particle-hole operators $A^\dagger_{ph}$ and A_{ph} of Eq. (76) (we shall not indicate angular-momentum coupling, for brevity) and the one-boson states $|\nu\rangle$ generated by the RPA operators $O^\dagger_\nu$ of Eq. (77). One can also define two-boson states by acting twice with RPA operators:

$$|\nu_1\nu_2\rangle \equiv \frac{1}{\sqrt{1+\delta_{\nu_1\nu_2}}} O^\dagger_{\nu_1} O^\dagger_{\nu_2} |\mathrm{RPA}\rangle \ . \tag{90}$$

The set of one-boson and two-boson states can be used as a basis to construct eigenstates of H of the form:

$$|\psi\rangle = \sum_\nu a_\nu |\nu\rangle + \sum_{\nu_1\nu_2} b_{\nu_1\nu_2} |\nu_1\nu_2\rangle \ . \tag{91}$$

These eigenstates would be found by diagonalizing H in the basis of $|\nu\rangle$ and $|\nu_1\nu_2\rangle$ states.

The construction of the secular matrix to be diagonalized can be facilitated if one uses a boson mapping between Fermion operators and Boson operators and if one truncates the mapping at lowest order. Denoting by $A^\dagger, A$ the Fermion operators and by $\hat{A}^\dagger, \hat{A}$ the corresponding Boson operators, the following mapping was used in Ref. 44):

$$\begin{aligned} A^\dagger_{ph} &\longrightarrow \hat{A}^\dagger_{ph}, \\ A^\dagger_{pp'} &\longrightarrow \sum_{h''} \hat{A}^\dagger_{ph''} \hat{A}_{ph''}, \\ A^\dagger_{hh'} &\longrightarrow \delta_{hh'} - \sum_{p''} \hat{A}^\dagger_{p''h'} \hat{A}_{p''h} \ . \end{aligned} \tag{92}$$

Since the Hamiltonian H can be expressed in terms of the operators $A^\dagger_{ph}, A^\dagger_{pp'}, A^\dagger_{hh'}$ and their hermitian conjugates, the mapping (92) gives a Hamiltonian $\hat{H}$ acting in Boson space. The same mapping is used to replace the Fermion operators $O^\dagger_\nu$ by Boson operators and finally the matrix elements of $\hat{H}$ in one- and two-boson space can be obtained. These matrix elements depend of course on two-body matrix elements of the Coulomb force, and also on the RPA amplitudes X and Y. The fact that Y-amplitudes are non-negligible results in appreciable coupling among two-boson states, and also between one- and two-boson states. As a result, the spectrum of eigenvalues of $\hat{H}$ is far from being harmonic. In Fig. 22, the spectrum of 0^+, 2^+ and 4^+ states obtained by combining plasmon excitations of multipolarity 0, 1 and 2 (denoted by M, D and Q, respectively) in the cluster Na^+_{21} is shown. The large differences between the unperturbed one- and two-boson spectrum and the eigenvalues of the diagonalized Hamiltonian show the strong anharmonicity effects. The origin of these effects is the same as in the case of the ground state correlations, namely the large backward amplitudes Y which are due ultimately to the long range nature of the interaction, as discussed in the previous subsection.

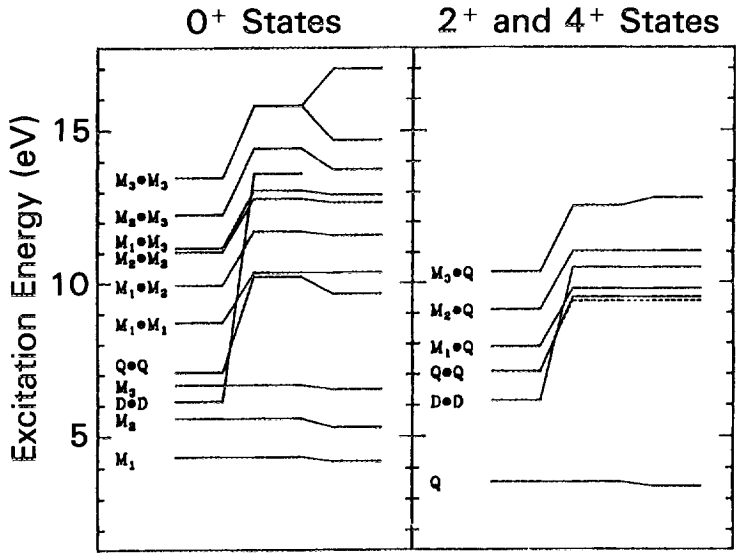

Fig. 22. Positive parity states in Na_{21}^{+} cluster calculated in one-boson plus two-boson space. Labels M, D and Q stand for monopole, dipole and quadrupole, respectively. Left columns: spectra of non-interacting bosons; middle columns: displacements caused by diagonal matrix elements; right columns: results of Hamiltonian diagonalization.

§6. Bulk plasmon energy in alkali metals

We have seen in the preceding sections that core effects of the atoms constituting the clusters play an important role in modifying the plasmon frequency and other electronic properties. In particular, the non-locality effects introduced either by a truly non-local pseudopotential or by the momentum dependence of pseudohamiltonians give rise to an effective mass for the valence electrons. In the bulk system, i.e., in the homogeneous electron gas it is possible to study in an analytical way the connection between the non-local components of the core potentials, the effective mass of valence electrons and their optical mass which ultimately determines the bulk plasmon energy. It is therefore interesting to apply the jellium model with pseudohamiltonians or pseudopotentials to the bulk system.

Let us consider a gas of N interacting valence electrons in an external ionic potential $\hat{v}$ defined by:

$$\hat{v} = \lim_{N,\Omega\to\infty} \frac{N}{\Omega} \int_{\Omega} v_{e\text{-}i} d^3 r_I \ , \tag{93}$$

where the limit is taken such that $\frac{N}{\Omega} = n_0 = \frac{3}{4\pi r_s^3}$ (the static bulk density). In the plain JM $v_{e\text{-}i}$ is simply the Coulomb interaction $-e^2/|\boldsymbol{r} - \boldsymbol{r}_I|$. In the PPJM or PHJM models, $v_{e\text{-}i}$ is the non-local potential (7) or the pseudohamiltonian (9), respectively. Suppose that the electrons are submitted to an external oscillating field $\lambda(G^{\dagger}e^{-i\omega t} + Ge^{i\omega t})$. Then, the time-dependent Kohn-Sham equations are:

$$i\frac{\partial}{\partial t}\phi_i(\boldsymbol{r},t) = \Bigg[-\frac{1}{2}\nabla_r^2 + \int d^3r' \frac{\rho(\mathbf{r}',t)}{|\boldsymbol{r}-\boldsymbol{r}'|} + \hat{v} + v_{x,c}(\rho(\boldsymbol{r},t)) + \lambda(G^\dagger e^{-i\omega t} + Ge^{+i\omega t})\Bigg]\phi_i(\boldsymbol{r},t) \ , \tag{94}$$

where

$$\rho(\boldsymbol{r},t) = \sum_{i=1}^{N} |\phi_i(\boldsymbol{r},t)|^2 \ , \tag{95}$$

and $v_{xc} = \delta E_{xc}/\delta\rho$ (see Eq. (28). In the infinite system, due to translational invariance, one has $G = e^{-i\boldsymbol{q}\cdot\boldsymbol{r}}$ and Eq. (94) gives rise to solutions of the form

$$\rho(\boldsymbol{r},t) = \rho_0 + \delta\rho(e^{i(\boldsymbol{q}\cdot\boldsymbol{r}-\omega t)} - e^{-i(\boldsymbol{q}\cdot\boldsymbol{r}-\omega t)}) \ , \tag{96}$$

where $\delta\rho$ is a constant to be determined and $\rho_0 = n_0$. The dynamic polarizability relative to the excitation operator $F = \sum_i^N e^{i\boldsymbol{q}\cdot\boldsymbol{r}_i}$ is given by [45]

$$\chi(F,G;\omega)_{\mathrm{TDLDA}} = \frac{F_+(\omega)}{\lambda} \ , \tag{97}$$

where $F_+(\omega)$ is defined by

$$\begin{aligned}\delta F(t) &\equiv \int d^3r e^{i\boldsymbol{q}\cdot\boldsymbol{r}}\delta\rho(\boldsymbol{r},t) \\ &= F_+e^{i\omega t} + F_-e^{-i\omega t} \ ,\end{aligned} \tag{98}$$

where $\delta\rho(\boldsymbol{r},t) = \rho(\boldsymbol{r},t) - \rho_0$. Using Eq. (96) one then gets

$$\begin{aligned}\chi(F,G;\omega)_{\mathrm{TDLDA}} &= \frac{1}{\lambda}\int d^3r e^{i\boldsymbol{q}\cdot\boldsymbol{r}}\delta\rho e^{-i\boldsymbol{q}\cdot\boldsymbol{r}} \\ &= \frac{1}{\lambda}\Omega\delta\rho \ .\end{aligned} \tag{99}$$

We now proceed to write down the explicit expression of the dynamic polarizability. Let us define the density dependent potential $V_{\mathrm{TDLDA}}(\boldsymbol{r},\rho(\boldsymbol{r},t))$ of Eq. (94):

$$V_{\mathrm{TDLDA}}(\boldsymbol{r},\rho(\boldsymbol{r},t)) = \int d^3r' \frac{\rho(\boldsymbol{r}',t)}{|\boldsymbol{r}-\boldsymbol{r}'|} + v_{x,c}(\rho(\boldsymbol{r},t)) \ . \tag{100}$$

Inserting the solution (96) in Eq. (100), one gets up to terms linear in $\delta\rho(\boldsymbol{r},t)$:

$$V_{\mathrm{TDLDA}}(\boldsymbol{r},\rho(\boldsymbol{r},t)) = V_{\mathrm{LDA}}(\rho_0) + \left[\frac{\partial V_{\mathrm{TDLDA}}}{\partial\rho}\right]_{\rho=\rho_0}\delta\rho(\boldsymbol{r},t) \ , \tag{101}$$

where ρ_0 and $V_{\mathrm{LDA}}(\rho_0)$ are the static density and potential, respectively. From Eqs. (101) and (96) one gets

$$V_{\mathrm{TDLDA}}(\boldsymbol{r},\rho(\boldsymbol{r},t)) = V_{\mathrm{LDA}}(\rho_0) + \left[\int d^3r' \frac{e^{i\boldsymbol{q}\cdot(\boldsymbol{r}'-\boldsymbol{r})}}{|\boldsymbol{r}-\boldsymbol{r}'|} + \left(\frac{\partial v_{x,c}}{\partial\rho}\right)_{\rho=\rho_0}\right]\delta\rho(e^{i(\boldsymbol{q}\cdot\boldsymbol{r}-\omega t)} + \text{c.c.})$$
$$= V_{\mathrm{LDA}}(\rho_0) + \left[\frac{4\pi}{q^2} + \left(\frac{\partial v_{x,c}}{\partial\rho}\right)_{\rho=\rho_0}\right]\delta\rho(e^{i(\boldsymbol{q}\cdot\boldsymbol{r}-\omega t)} + \text{c.c.}) \ . \tag{102}$$

The TDLDA equations assume now the following form:

$$i\frac{\partial}{\partial t}\phi_i(\boldsymbol{r},t) = \left[-\frac{1}{2}\nabla_{\boldsymbol{r}}^2 + V_{\mathrm{LDA}}(\rho_0) + \hat{v} + \left(\left[\frac{4\pi}{q^2} + \left(\frac{\partial v_{x,c}}{\partial\rho}\right)_{\rho=\rho_0}\right]\delta\rho + \lambda\right)(e^{i(\boldsymbol{q}\cdot\boldsymbol{r}-\omega t)} + \text{c.c.})\right]\phi_i(\boldsymbol{r},t)$$
$$= \left[-\frac{1}{2}\nabla_{\boldsymbol{r}}^2 + V_{\mathrm{LDA}}(\rho_0) + \hat{v} + \lambda'(q)(e^{i(\boldsymbol{q}\cdot\boldsymbol{r}-\omega t)} + \text{c.c.})\right]\phi_i(\boldsymbol{r},t) \ , \tag{103}$$

where we have defined

$$\lambda'(q) = \lambda + \left[\frac{4\pi}{q^2} + \left(\frac{\partial v_{x,c}}{\partial\rho}\right)_{\rho=\rho_0}\right]\delta\rho \ . \tag{104}$$

Equations (103) are now TDLDA equations for a non-interacting (single-particle) gas of electrons in a static field $V_{\mathrm{LDA}}(\rho_0) + \hat{v}$ and submitted to a new external field $\lambda'(q)(e^{i(\boldsymbol{q}\cdot\boldsymbol{r}-\omega t)} + \text{c.c.})$ with coupling constant $\lambda'(q)$ given by Eq. (104). The dynamic polarizability corresponding to these equations is the single-particle response function:

$$\chi^0(q,\omega) = 2\sum_{m,i}\varepsilon_{m,i}\frac{|\langle m|e^{i\boldsymbol{q}\cdot\boldsymbol{r}}|i\rangle|^2}{(\omega+i\eta)^2-\varepsilon_{mi}} \ . \tag{105}$$

The single-particle (-hole) states $|m\rangle(|i\rangle)$ and excitation energies ε_{mi} are built with the solutions of the static Kohn-Sham equations (27). From the result (99) for the TDLDA polarizability and the analogous relation for χ^0:

$$\chi^0(q,\omega) = \frac{1}{\lambda'(q)}\Omega\delta\rho \ , \tag{106}$$

one then gets

$$\lambda\chi_{\mathrm{TDLDA}} = \lambda'(q)\chi^0 \ = \ \Omega\delta\rho \ , \tag{107}$$

and therefore

$$\chi(q,\omega)_{\mathrm{TDLDA}} = \frac{\chi^0(q,\omega)}{1-\frac{1}{\Omega}\left[\frac{4\pi}{q^2}+\frac{\partial v_{x,c}}{\partial\rho}|_{\rho=\rho_0}\right]\chi^0(q,\omega)} \ . \tag{108}$$

The energy of the bulk plasmon can be derived by solving the equation

$$\chi^0(q,\omega) = \frac{\Omega}{\frac{4\pi}{q^2} + \frac{\partial v_{x,c}}{\partial \rho}|_{\rho=\rho_0}} , \tag{109}$$

which gives the poles of $\chi(q,\omega)_{\mathrm{TDLDA}}$. In the following we will focus on the $q \to 0$ limit of Eq. (109). In this limit one can neglect in Eq. (109) the exchange-correlation term with respect to the Coulomb one and consider the limiting case $\omega \gg \varepsilon_{mi}$ in the evaluation of $\chi^0(q,\omega)$ since only this part of $\chi^0(q,\omega)$ becomes relevant for the collective solution of Eq. (109), as it is apparent from the graphical solution of Eq. (109). From Eq. (105), for $\omega \gg \varepsilon_{mi}$ one gets

$$\chi^0(q,\omega) \simeq \frac{2}{\omega^2} m_1^{sp}(q) , \tag{110}$$

where m_1^{sp} is the energy-weighted sum rule

$$\begin{aligned} m_1^{sp} &\equiv \sum_{mi} \varepsilon_{mi} |\langle m|e^{i\boldsymbol{q}\cdot\boldsymbol{r}}|i\rangle|^2 \\ &= \frac{1}{2}\langle \mathrm{KS}|[\sum_i e^{-i\boldsymbol{q}\cdot\boldsymbol{r}_i}, [H_0, \sum_i e^{i\boldsymbol{q}\cdot\boldsymbol{r}_i}]]|\mathrm{KS}\rangle . \end{aligned} \tag{111}$$

From Eqs. (109) and (110) one finally gets:

$$\frac{2}{\omega^2} m_1^{sp}(q) = \frac{\Omega}{4\pi} q^2 . \tag{112}$$

Equation (112) is a general result valid in the $q \to 0$ limit. Evaluation of m_1^{sp} in different models yields to different predictions for the energy of the bulk plasmon. In the plain JM one has the well known result

$$m_1^{\mathrm{JM}} = \frac{Nq^2}{2} , \tag{113}$$

which follows immediately from the fact that in the jellium model the only term of H_0 contributing to the commutator (111) is the kinetic energy term. In the PPJM and PHJM the non-local terms of the electron-ion potential give rise, for both pseudopotential and pseudohamiltonian cases, to corrections to the result (113). At first sight these corrections might appear surprising since the true Hamiltonian has no momentum dependence and satisfies the energy-weighted sum rule. However, the number of electrons entering in the sum rule is in principle the total number (valence plus core) of electrons and not only the number N of valence electrons as in Eq. (113). In the PPJM and PHJM one takes into account only the valence electrons, as in the jellium model, but differently from the jellium, core electrons are simulated with an effective valence electron-ion interaction. We expect that the jellium models will describe the excitation strength and then the energy-weighted sum rule correctly in the low energy region. At energies much higher than the plasmon, there would be additional excitation strength not contained in these jellium models, restoring the sum rule result with the true Hamiltonian.

In the bulk system the m_1^{sp} sum rule can also be calculated analytically for PHJM and PPJM, and it takes the form:[11]

$$m_1^{\mathrm{PH}} = \frac{Nq^2}{2}\left[1 + \rho_0 \int \left(a(r) + \frac{2}{3}b(r)\right) d^3r\right] \tag{114}$$

and

$$m_1^{\mathrm{PP}} = \frac{Nq^2}{2}\left[1 - \frac{4}{3\pi}k_F^2 \int \bar{\Delta}(x)x^3 j_1(k_F x)dx\right] , \tag{115}$$

where

$$\bar{\Delta}(x) = \frac{2}{\pi}\sum_{l}^{l_{\max}}(2l+1)\int q^2 dq x'^2 dx' j_0(qx)(j_l(qx'))^2 v_l(x') , \tag{116}$$

and the $j_l(qx)$ are spherical Bessel functions. From Eqs. (112)$\sim$(116) one gets for the energy ω_p of the bulk plasmon the result

$$\omega_p = \sqrt{\frac{4\pi\rho_0}{m_{\mathrm{opt}}}} , \tag{117}$$

where the inverse optical mass $1/m_{\mathrm{opt}}$ is equal to 1 in the jellium model and given by

$$\frac{1}{m_{\mathrm{opt}}^{\mathrm{PH}}} = 1 + \rho_0 \int d^3r \left(a(r) + \frac{2}{3}b(r)\right) \tag{118}$$

and

$$\frac{1}{m_{\mathrm{opt}}^{\mathrm{PP}}} = 1 - \frac{4}{3\pi}k_F^2 \int \bar{\Delta}(x)x^3 j_1(k_F x)dx \tag{119}$$

for the pseudohamiltonian and pseudopotential, respectively.

In Table V are reported the predictions of the different models for the optical mass and for the bulk plasmon energy of alkali metals together with the experimental results. From Table V one can see that the predictions of PHJM and PPJM do not coincide and are particularly different in the case of Lithium where non-local effects are more important. One way to obtain an improved pseudohamiltonian giving

Table V. Optical masses and bulk plasmon energies (in eV) of alkali metals in the PPJM (PP) and PHJM (PH). Experimental values for Li are from Refs. 47) and 48), for the rest of alkalis see Ref. 49). Calculated results are from Ref. 11).

	$m_{\mathrm{opt}}^{\mathrm{PP}}$	$m_{\mathrm{opt}}^{\mathrm{PH}}$	ω_p^{PP}	ω_p^{PH}	ω_p^{exp}
Li	1.155	1.526	7.48	6.51	6.7
Na	1.051	1.040	5.90	5.93	5.72
K	1.017	0.983	4.36	4.44	3.72
Rb	0.980	0.909	4.01	4.17	3.41
Cs	1.015	0.872	3.51	3.79	2.99

bulk plasmon properties closer to the predictions of the pseudopotential would be to impose the same local part for both pseudopotential and pseudohamiltonian while the non-local parts are treated differently in each case. Table V shows that the predicted plasmon energies are systematically higher than the experimental values. It must be recalled[46] that a lowering of calculated plasmon energies in the series Na to Cs originates from band structures effects which are not accounted for in the present jellium approach. On the other hand, a large discrepancy in the case of Li with PPJM still remains.

In summary, we have seen that the value of the optical mass depends on the particular model (pseudopotential or pseudohamiltonian) used for the core potential when non-local effects are important and the optical mass deviates from the bare mass. As a consequence, it is found that the predicted value for the energy of the bulk plasmon varies considerably from one model to another in the case of Lithium. This result seems to be a feature only of infinite systems while in (small) finite size systems, like clusters of alkali metals, the different models still give quite similar predictions for the position of the plasmon resonance.[9] This is due to the fact that, differently from the bulk case, in finite systems the local parts of the pseudopotential and pseudohamiltonian play a crucial role and cancel out the differences between the two models originating from the different non-local components.

§7. Concluding remarks

We have done a quick survey of electronic properties of metal clusters studied in the framework of density functional theory and the jellium models. We have concentrated on some recent works aimed at stressing the effects of interactions between valence electrons and ionic cores, and we have seen that a better description of these interactions in terms of pseudohamiltonians or pseudopotentials can improve our understanding of experimental results.

The present survey is, by far, not exhaustive and many aspects of metal cluster physics have not been treated, such as deformations in clusters, temperature effects on dipole plasmons, fission processes, etc. All these aspects are also very important and they constitute a wide field of applications for the density functional approach in conjunction with the jellium model.

Future progress in the density functional description of atomic clusters would require a more refined picture of the ionic background going beyond the uniform jellium. Ionic lattice effects can be in some cases important and should be treated explicitly. Improvements in this direction will involve, however, a considerable numerical effort as compared to the simplifications brought by the jellium assumption. In spite of its limitations and drawbacks, the jellium model thus remains a powerful tool to understand electronic properties of atomic clusters up to the largest sizes.

Acknowledgements

This review is are based on works done in collaboration, and numerous discussions with G. B. Bachelet, F. Catara, Ph. Chomaz, E. Lipparini, Ll. Serra and C.

Yannouleas. I would like to express my heartiest thanks to them all.

References

1) W. D. Knight, K. Clemenger, W. A. de Heer, W. A. Saunders, M. Y. Chou and M. L. Cohen, Phys. Rev. Lett. **52** (1984), 2141.
2) W. D. Knight, K. Clemenger, W. A. de Heer and W. A. Saunders, Phys. Rev. **B31** (1985), 2539.
3) G. D. Mahan and K. R. Subbaswamy, *Local Density Theory of Polarizability* (Plenum Press, New York, 1990).
4) W. Ekardt, Phys. Rev. **B31** (1985), 6360.
5) W. A. de Heer, Rev. Mod. Phys. **65** (1993), 611.
6) M. Brack, Rev. Mod. Phys. **65** (1993), 677.
7) W. Ekardt and Z. Penzar, Phys. Rev. **B43** (1991), 1322.
8) G. B. Bachelet, D. R.Hamann and M. Schlüter, Phys. Rev. **B26** (1982), 4199.
9) F. Alasia, Ll. Serra, R. A. Broglia, N. Van Giai, E. Lipparini and H. E. Roman, Phys. Rev. **B52** (1995-I), 8488.
10) G. B. Bachelet, D. M. Ceperley and M. G. B. Chiocchetti, Phys. Rev. Lett. **62** (1989), 2088.
11) E. Lipparini, N. Van Giai and Ll. Serra, J. of Phys.:Condens.Matter **7** (1995), 4467.
12) Ll. Serra, G. B. Bachelet, N. Van Giai and E. Lipparini, Phys. Rev. **B48** (1993 - I), 14708.
13) P. A. M. Dirac, Proc. Cambridge Philos. Soc. **26** (1930), 376.
14) E. P. Wigner, Phys. Rev. **46** (1934), 1002.
15) O. Gunnarsson and B. I. Lundqvist, Phys. Rev. **B13** (1976), 4274.
16) W. D. Knight, W. A. de Heer, K. Clemenger and W. A. Saunders, Solid State Commun. **53** (1985), 445.
17) N. D. Lang and W. Kohn, Phys. Rev. **3** (1971), 1215.
18) C. Bréchignac, Ph. Cahuzac, F. Carlier, Y. Leygnier, J. Ph. Roux and A. Sarfati, contribution to ISSPIC6, Chicago (1992).
19) O. Genzken and M. Brack, Phys. Rev. Lett. **67** (1991), 3286.
20) H. Nishioka, K. Hansen and B. R. Mottelson, Phys. Rev. **B42** (1990 - II), 9377.
21) F. Catara, Ph. Chomaz and N. Van Giai, Z. Phys. **D33** (1995), 219.
22) C. Bréchignac et al., Phys. Rev. **B47** (1993 - II), 2271.
23) A. L. Fetter and J. D. Walecka, *Quantum Theory of Many Particle Systems* (McGraw Hill, New York, 1971).
24) P. Ring and P. Schuck, *The Nuclear Many Body Problem* (Springer, Berlin, 1982).
25) G. F. Bertsch and S. F. Tsai, Phys. Rep. **18C** (1975), 126.
26) R. Courant and D. Hilbert, *Methods of Mathematical Physics* (Interscience Publishers, 1953).
27) Ll. Serra, E. Lipparini and N. Van Giai, Europhys. Lett. **29** (1995), 445.
28) C. Bréchignac, Ph. Cahuzac, N. Kebaili, Y. Leygnier and A. Sarfati, Phys. Rev. Lett. **68** (1992), 3916.
29) S. Pollack, C. R. C. Wang and M. M. Kappes, J. Chem. Phys. **94** (1991), 2496.
30) C. Bréchignac, Ph. Cahuzac, Y. Leygnier and A. Sarfati, Phys. Rev. Lett. **70** (1993), 2036.
31) G. Mie, Ann. Phys. (Leipzig) **25** (1908), 377.
32) D. R. Snider and R. S. Sorbello, Phys. Rev. **B28** (1983), 5702.
33) N. D. Lang and W. Kohn, Phys. Rev. **B7** (1973), 3541.
34) C. Yannouleas, F. Catara and N. Van Giai, Phys. Rev. **B51** (1995 - I), 4569.
35) W. A. Saunders, Phys. Rev. **A46** (1992), 7028.
36) L. Brey, N. F. Johnson and B. I. Halperin, Phys. Rev. **B40** (1989), 10647.
37) J. Dempsey and B. I. Halperin, Phys. Rev. **B47** (1993), 4662.
38) E. A. Sanderson, Phys. Lett. **19** (1965), 141.
39) D. Agassi, V. Gillet and A. Lumbroso, Nucl. Phys. **A130** (1969), 129.
40) C. Yannouleas and R. A. Broglia, Ann. of Phys. **217** (1992), 105.
41) C. Yannouleas and R. A. Broglia, Phys. Rev. **A44** (1991), 5793.
42) C. Yannouleas, E. Vigezzi and R. A. Broglia, Phys. Rev. **B47** (1993), 9849.
43) J. Ritman et al., Phys. Rev. Lett. **70** (1993), 533.
44) F. Catara, Ph. Chomaz and N. Van Giai, Phys. Rev. **B48** (1993 -II), 18207.

45) D. Pines and P. Nozières, *The Theory of Quantum Liquids* (New York, Benjamin, 1966), vol. 1.
46) F. Aryasetiawan and K. Karlsson, Phys. Rev. Lett. **73** (1994), 1679.
47) M. Rasigni and G. Rasigni, J. Opt. Soc. Am. **67** (1974), 54.
48) T. A. Callcott and E. T. Arakawa, J. Opt. Soc. Am. **64** (1974), 839.
49) A. Von Felde, J. Sprosser-Prou and J. Fink, Phys. Rev. **B40** (1989), 10181.